Reactive nitrogen in and around the northeastern and Mid-Atlantic US: sources, sinks, and connections with ozone

Min Huang[1,2], Gregory R. Carmichael[3], James H. Crawford[4], Kevin W. Bowman[5], Isabelle De Smedt[6], Andreas Colliander[5], Michael H. Cosh[7], Sujay V. Kumar[1], Alex B. Guenther[8], Scott J. Janz[1], Ryan M. Stauffer[1], Anne M. Thompson[1], Niko M. Fedkin[1], Robert J. Swap[1], John D. Bolten[1], Alicia T. Joseph[1]

[1]Earth Sciences Division, NASA Goddard Space Flight Center, Greenbelt, MD 20771, USA
[2]Earth System Science Interdisciplinary Center, University of Maryland, College Park, MD 20740, USA
[3]College of Engineering, University of Iowa, Iowa City, IA 52242, USA
[4]Science Directorate, NASA Langley Research Center, Hampton, VA 23666, USA
[5]Jet Propulsion Laboratory, California Institute of Technology, Pasadena, CA 91109, USA
[6]Royal Belgian Institute for Space Aeronomy, 1180 Brussels, Belgium
[7]Hydrology and Remote Sensing Laboratory, US Department of Agriculture, Beltsville, MD 20705, USA
[8]Department of Earth System Science, University of California at Irvine, Irvine, CA 92697, USA

Correspondence to: Min Huang (minhuang@umd.edu)

Abstract. This study applies a regional Earth system model (NASA-Unified Weather Research and Forecasting with online chemistry) with updated parameterizations for selected land-air exchange processes and multi-platform observations, to first estimate reactive nitrogen (Nr = oxidized NO_y + reduced NH_x) emissions from anthropogenic and natural sources, nitrogen dioxide (NO_2) column densities and surface concentrations, total and speciated Nr dry or/and wet deposition fluxes during 2018–2023 over the northeastern and Mid-Atlantic US most of which belong to nitrogen oxides-limited or transitional chemical regimes. The estimated multi-year Nr concentrations and deposition fluxes are then compared with and related to ozone (O_3), in terms of their spatiotemporal variability and key drivers as well as possible ecosystem impacts. Finally, through three sets of case studies, we identify and discuss about 1) the capability of land data assimilation (DA) to reduce the uncertainty in modeled land surface states at daily-to-interannual timescales, that can propagate into atmospheric chemistry fields; 2) the impacts of irrigation on land surface and atmospheric fields as well as pollutants' ecosystem uptake and impacts; and 3) the impacts of transboundary air pollution during selected extreme events on pollutants' budgets and ecosystem impacts. With the updated model parameterizations and anthropogenic emission inputs, the eastern US surface O_3 modeled by this tool persistently agrees better with observations (i.e., with root-mean-square errors staying within 4–7 ppbv for the individual years' May-June-July) than those in literature where model errors often exceed 20 ppbv. Based on model calculations, surface O_3 correlates more strongly with early afternoon NO_2 columns than formaldehyde columns (r=0.54 and 0.40, respectively). The O_3 vegetative uptake overall dropped by ~10% from 2018 to 2023, displaying clearer downward temporal changes than the total Nr deposition due to the declining NO_y emission and deposition fluxes competing with the increasing NH_x fluxes. It is highlighted that, temporal variability of Nr and O_3 concentrations and fluxes on subregional-to-local scales respond to hydrological variability that can be influenced by precipitation and controllable human activities such as irrigation. Deposition processes and biogenic emissions that are highly sensitive to interconnected environmental and

35 plants' physiological conditions, as well as extra-regional sources (e.g., O_3-rich stratospheric air and dense wildfire plumes from upwind regions), have been playing increasingly important roles in controlling pollutants' budgets in this area as local emissions go down owing to effective emission regulations and COVID lockdowns. To better inform the design of mitigation and adaptation strategies, it is recommended to continue evaluating and improving the model parameterizations and inputs relevant to these processes in seamlessly coupled multiscale Earth system models using laboratory and field

40 experiments in combination with satellite DA which would in turn benefit remote sensing communities.

1 Background, motivation, and goals

Consisting of nitric oxide (NO) and nitrogen dioxide (NO_2), a US Environmental Protection Agency (EPA)-regulated criteria air pollutant that has the highest exposure disparities (Liu et al., 2021), nitrogen oxides (NO_x) are an important group of ozone (O_3) precursor and destroyer, and ground-level O_3 is another EPA-regulated criteria air pollutant. Emitted from various anthropogenic (anth) and natural sources, NO_x is readily transformable to/from other forms of reactive nitrogen (Nr = oxidized NO_y + reduced NH_x) species, such as ammonia (NH_3), peroxyacetyl nitrate (PAN) and nitric acid (HNO_3). Some of these chemical reactions also contribute to fine particulate matter pollution that connects with O_3 via the aerosol radiative effects and heterogeneous chemistry (Seinfeld and Pandis, 2016; Monks et al., 2021). Many previous studies have demonstrated that NO_x emissions and concentrations play more crucial roles than volatile organic compounds (VOCs) in regulating the magnitude and spatiotemporal variability of O_3 (e.g., Duncan et al., 2010; Jin et al., 2017; Koplitz et al., 2022; Souri et al., 2023) as well as aerosols (Carlton et al., 2010; Holt et al., 2015) in much of the northeastern and Mid-Atlantic states, the most populous US region where the land surface is highly heterogeneous and hydroclimatic extremes and exceedances of the US National Ambient Air Quality Standards occur from time to time (US Global Change Research Program, 2023; US EPA, 2023a). An improved understanding of the sources, sinks, and distributions of NO_x and Nr as well as how these have been and will be changing through time would be beneficial for interpreting O_3 air pollution levels and their spatiotemporal variability in this area. The removals of Nr, O_3, and other chemicals involved in their life cycles from the atmosphere through wet or/and dry deposition, closely interact with multiple other interconnected environmental stressors such as temperature, humidity, precipitation, soil moisture (SM) and carbon dioxide (CO_2) concentration as well as plants' physiological conditions. Together, they can cause intertwined and cascading effects on the diverse terrestrial and aquatic ecosystems (e.g., United Nations Economic Commission for Europe, 1999; Galloway et al., 2003, 2004; Felzer et al., 2009; Simpson et al., 2014; Lombardozzi et al., 2015; Mills et al., 2018; Walker et al., 2019; Clifton et al., 2020; Emberson, 2020) in this area. As anth emissions continue to decrease there due to effective environmental regulations and unusual situations such as COVID lockdowns, for studies on Nr and O_3, attention should also be given to quantifying the impacts of multiple climatic factors as well as nonlocal air pollution sources such as those imported from upwind US regions, Canada, and the stratosphere, which are partially controlled by the Bermuda High and other pressure systems (e.g., Colarco et al., 2004; Zhu et al., 2013; Ott et al., 2016; Rogers et al., 2020).

Previous global and regional modeling studies have shown that reproducing the observed warm-season Nr and surface O_3 levels in the US East is challenging, and the estimated background O_3 as well as the importance of its individual contributors varies substantially among models (e.g., Fiore et al., 2009; Chai et al., 2007, 2013; Lapina et al., 2014; Huang et al., 2017a; Lin et al., 2017). Often, the large model-observation mismatches of 20 ppbv or higher in surface O_3 were not well explained or attributed mainly to the models' uncertain/outdated anth emission inputs. Some of these studies implemented advanced chemical data assimilation (DA) methods to reduce the errors in their predicted surface O_3 states by ~50% (Chai et al.,

2007), but did not improve the mechanistic representations of O₃ related processes which are of higher policy-relevance and

75   would lengthen the impacts of chemical DA since the model initializations/analysis times. The large uncertainty in model results limits the capability of understanding air quality there and evaluating potential strategies to mitigate the air pollution impacts. High-resolution Earth system modeling with proper model parameterizations, up-to-date inputs, and comprehensive, process-based analysis aided by cross-disciplinary observations is anticipated to help elucidate the various factors controlling Nr and O₃ (Fig. 1a) to better assist with assessing their environmental impacts from past to future.

80

In support of the International Global Atmospheric Chemistry-Tropospheric Ozone Assessment Report (TOAR) phase II activity which aims to further examine the distributions, temporal changes, and impacts of O₃ and its key precursors, this study applies a regional Earth system model with updated parameterizations for selected land-atmosphere exchange processes (Section 2.1), running over the Northeast and Mid-Atlantic states for multiple years at 10 km horizontal resolution

85   that is considered to be able to better capture NOₓ lifetime and budgets than coarser resolution systems (Li et al., 2023). The model is used together with multiplatform, multidisciplinary observations (Section 2.2) and a range of analysis methods (e.g., model evaluation and diagnosis, formal DA, and sensitivity simulations, Section 2.3) to help achieve the following specific goals: 1) to estimate Nr emissions from various anth and natural (e.g., soil NO and nitrous acid, HONO) sources, NO₂ surface concentrations and column densities, total and speciated Nr dry or/and wet deposition fluxes during 2018–2023,

90   with discussions on key anth and environmental/climatic drivers of their spatiotemporal variability during this period (Section 3.1); 2) to compare and relate Nr and O₃ concentrations as well as their deposition fluxes during 2018–2023, in terms of spatiotemporal variability, reactions to environmental and biophysical stresses, and potential ecosystem impacts (Section 3.2); and 3) through three sets of case studies, to demonstrate and discuss in detail about: the capability of land DA to reduce the uncertainty in the modeled land surface states, land-atmosphere exchange processes and atmospheric states at

95   daily-to-interannual timescales; the impacts of controllable human activities such as irrigation on land surface and atmospheric fields and pollutants' ecosystem uptake; and the impacts of transboundary air pollution during selected extreme events on pollutants' budgets and ecosystem impacts (Section 3.3). These case studies also help identify sources of model uncertainty before we draw conclusions and outline future directions for further advancements in related areas in Section 4.

2 Methods

100   ### 2.1 Coupled modeling system and the baseline simulation

On a 10 km, 63 vertical layer Lambert conformal grid (Fig. 1b–c) from the subsurface to ~100 hPa, the NASA-Unified Weather Research and Forecasting model with online chemistry (WRF-Chem) simulations were conducted over the Northeast and Mid-Atlantic states for 2018–2023 growing seasons starting from late April of each year. The analysis of the baseline simulation was focused on May-June-July (MJJ) of 2018–2020, 2022, and 2023. MJJ falls within the plant growing

105   and O₃ seasons when atmospheric Nr and O₃ most actively interact with ecosystems (Li et al., 2015; Clifton et al., 2020).

Year of 2021 is not an emphasis in this paper partly due to the lack of reliable information to represent the COVID impacts on anth emissions for that year. The four-layer Noah-Multiparameterization (MP, Niu et al., 2011) land surface model (LSM) version 3.6 within the NASA Land Information System served as the land component of this modeling system, running with a sprinkler irrigation and the Community Land Model type of SM factor controlling stomatal resistance (i.e., β
110 factor) schemes. Noah-MP was forced by the North American Land Data Assimilation System Phase 2 forcing data during the long-term (since 2000) offline spin-up. Noah-MP's CO_2 forcings for 2018, 2019, 2020, 2022, 2023's warm seasons were set to 410, 412, 415, 420, and 423 ppmv, respectively, based on measurements at the Mauna Loa Observatory and its nearby Maunakea Observatories for part of 2023 (https://gml.noaa.gov/webdata/ccgg/trends/co2/co2_mm_mlo.txt, last access: 12 January 2024). The land use/land cover (LULC) and soil type inputs of Noah-MP were based on the 20-category
115 International Geosphere-Biosphere Programme-modified Moderate Resolution Imaging Spectroradiometer (MODIS) and the 16-category State Soil Geographic (STATSGO) datasets, respectively (Fig. 1b–c). Crop-type and irrigation map/fraction information required by the irrigation scheme came from Monfreda et al. (2008) and Salmon et al. (2015), respectively, the latter of which incorporated MODIS information.

120 Major atmospheric and land model physics as well as chemistry schemes were configured in similar ways to those in Huang et al. (2022). The photosynthesis-based dry deposition approach recommended in Huang et al. (2022) and a number of other previous dry deposition studies cited therein was applied to most gaseous species. No change was made to sulfur dioxide dry deposition approach (Erisman et al., 1994) for this study. Wet deposition fluxes are also analyzed and discussed in this work. In replacement of the metric-based approach in Huang et al. (2022), O_3 vegetative impacts were dynamically modeled by
125 applying two separate factors to photosynthesis and stomatal conductance rates (Lombardozzi et al., 2015) that are calculated in Noah-MP. These factors are land cover-dependent functions of O_3 uptake cumulated during growing season when leaf area index (LAI) exceeds 0.5. To account for the ability of plants to detoxify O_3, O_3 fluxes were only accumulated when they exceeded a threshold of 1.0 nmol O_3 m^{-2} s^{-1}. As demonstrated in previous offline (Lombardozzi et al., 2015) and online (Li et al., 2016; Sadiq et al., 2017) modeling studies, dynamically modeling O_3 vegetative impacts could help quantify the
130 perturbations of O_3 to a variety of hydrological, ecological, and weather variables. Online-calculated biogenic emissions of O_3 precursors such as VOCs and Nr species in the simulations were adjusted to be more sensitive to multiple environmental stresses. Specifically, a drought adjusting factor γ_d was introduced in the Model of Emissions of Gases and Aerosols from Nature (MEGAN) biogenic isoprene emission calculations following the suggestions by Jiang et al. (2018), which depends on the β factor and the maximum carboxylation rate. The plant function type information needed for MEGAN was converted
135 from the annual European Space Agency Climate Change Initiative (ESA CCI) land cover product for 2018–2020, and 2020 data from this product were also used for the years afterwards. The Noah-MP modeled LAIv (i.e., LAI/Green Vegetation Fraction) feeds into MEGAN calculations. Soil emissions of NO were estimated largely based on the mechanism recommended by Hudman et al. (2012) and Simpson and Darras (2021), i.e., for dry and wet soils that are determined by a SM index (i.e., a function of SM, soil wilting point and field capacity), different sets of biome-based emission coefficients

140 (Steinkamp and Lawrence, 2011) and the standing Nr pool plus nitrogen input from deposition being adjusted by water-filled pore space θ (i.e., SM divided by porosity), soil temperature (Wang et al., 2021), and canopy reduction factor. The pulsing effects, which are small for this study area/season, were accounted for. Soil HONO emissions were also calculated online, scaled from soil NO emissions using biome-dependent factors specified in Table A1 of Rasool et al. (2019) that were partly adapted from Oswald et al. (2013). Nitrogen input from fertilizer was not included in the soil emissions calculations to avoid

145 double counting with agricultural emissions from the anth emission input to be introduced below. Oceanic natural NH_3 emissions were not included, which were estimated to have negligible impacts on Nr overland (Paulot et al., 2013). Lightning emissions were also calculated online and vertically distributed adopting the setup described in Huang et al. (2021) which was based on cloud-top-height-based parameterizations (Wong et al., 2013) and climatological intra-cloud to cloud-to-ground flash ratios. A passive lightning NO_x tracer was again implemented, that experienced atmospheric transport

150 but not chemical reactions. Aerosol direct, semidirect and indirect radiative effects were enabled.

Emissions from various anth source sectors came from the Copernicus Atmosphere Monitoring Service (CAMS) global inventory version 5.3, available at 0.1°×0.1° horizontal resolution with monthly and year-by-year variability. To account for COVID impacts, for 2020, grid- and sector-dependent factors (Doumbia et al., 2021) were applied to adjust the emissions.

155 This CAMS inventory for recent years was developed by extrapolating the Emissions Database for Global Atmospheric Research version 5 based on the Community Emissions Data System version 2 trends and including emissions from ships as well as monthly variability that were estimated separately (Granier et al., 2019; Soulie et al., 2023). Elguindi et al., (2020) noted that NO_x emissions for recent decades from an earlier version of CAMS inventory do not notably differ from other bottom-up inventories over the US where more detailed information for emission inventory developments are available. In

160 contrast, top-down estimates diverge significantly due to uncertainty in the used satellite NO_2 retrievals as well as the model representations of various atmospheric processes many of which are scale-dependent. A clear understanding of the impact of background NO_x sources, including natural emissions, on constraining NO_x emissions with satellite NO_2 data is urgently needed. The 0.1°×0.1°, version 2.6r1 of the Quick Fire Emissions Dataset (QFED, Darmenov and da Silva, 2015), developed with the fire radiative power approach, was applied with plume rise. Wiedinmyer et al. (2023) report that QFED NO_x

165 emissions over North America during 2012–2019 are in comparable magnitudes with other widely-used fire emission datasets while its NH_3 emissions are higher than the estimates from other products. Figure 2 presents the total anth and biomass burning (fire) NO_x and NH_3 emissions averaged for each year's MJJ. Anth NO_x emissions are shown to decrease due to effective emission controls (i.e., a -16.3% overall change from 2018 to 2023), except for slight increases along a few shipping lanes. They are anomalously low in 2020 (~23.8% lower than 2018) largely due to reduced human activities during

170 the COVID lockdowns. The temporal changes in non-methane (NM) VOC emissions are relatively smaller, with the domain-mean in 2023 only ~6% lower than in 2018. The total anth NH_3 emissions were growing in many places, most evidently over croplands as a result of the rising agricultural soil and livestock emissions. The QFED-based fire NO_x and NH_3 emissions were generally increasing, reaching their highest in 2023.

Daily reinitialized atmospheric initial conditions (ICs) and boundary conditions (BCs) were downscaled from the 3-hourly, 32 km North American Regional Reanalysis dataset. A set of the 6-hourly Community Atmosphere Model with Chemistry (CAM-Chem, for 2018–2020, 0.9°×1.25°/56 vertical levels) and Whole Atmosphere Community Climate Model (WACCM, beyond 2020, 0.9°×1.25°/88 vertical levels) simulations that also ingested QFED fire information served as the chemical BCs of the WRF-Chem baseline simulation because of its higher completeness of chemical species, and for WACCM, its availability for very recent years compared to chemical reanalysis products which are widely considered to be more accurate. The chemical BC models' stratospheric O_3 tracer fields also supported our multi-year analysis and a case study (Section 3.3). The interannual variability in lower free tropospheric O_3 (Fig. 3a, up to 10 ppbv) and its precursors upwind of the eastern US, as well as the synoptic wind fields (Fig. 3c, shifting from westerly in 2018–2022 to northwesterly in 2023), play critical roles in controlling the modeled large-scale O_3 patterns and their temporal changes. From 2018 to 2023, the lower free tropospheric O_3 in MJJ first hiked by up to 4 ppbv, and then dipped down by up to 4–6 ppbv before rising again. Under the largest stratospheric influences, transported background O_3 more strongly impacted the southern part of our domain in 2023 than in 2018 by up to 4 ppbv (Fig. 3a–b). Although the stratospheric air influences on surface O_3 were diluted to no more than a few ppbv (Fig. S1), the challenges regional models experience in reproducing their magnitudes and interannual variability may introduce uncertainty to the estimated surface O_3 changes.

2.2 Observations

2.2.1 Chemical observations from satellites and ozonesondes

The TROPOspheric Monitoring Instrument (TROPOMI) on board the Copernicus Sentinel-5 Precursor satellite launched in 2017 provides trace gas and aerosol measurements at daily global coverage since April 2018, with ascending node ~13:30 local time overpasses. It has much finer resolutions (i.e., 3.5×5.5 km^2 at nadir since August 2019, and 3.5×7 km^2 before then), a wider spectral range and higher signal-to-noise ratio per ground pixel than its predecessors. TROPOMI data have demonstrated their robustness in studying air pollution from numerous source sectors (e.g., land and water traffic, power plants, oil, gas and other industries, biogenic and fire) in greater detail (e.g., Georgoulias et al., 2020; van der Velde et al., 2021; Griffin et al., 2021; Goldberg et al., 2021; Dix et al., 2022). In this study, the gridded (0.02°×0.02°) monthly and daily level 2 TROPOMI tropospheric vertical column NO_2 data were analyzed together with WRF-Chem results to help understand temporal changes in column NO_2. The gridded (0.05°×0.05°) monthly TROPOMI formaldehyde (HCHO) tropospheric vertical columns (De Smedt et al., 2021) were also used to calculate HCHO/NO_2 ratios to help determine O_3 chemical regimes over the study area. The TROPOMI-based HCHO/NO_2 ratios were supplemented by those derived from the gridded (1 km×1 km) NO_2 and HCHO data collected on selected days of 2018 over New York City and the Long Island Sound by two similar airborne instruments Geostationary Trace gas and Aerosol Sensor Optimization (GeoTASO) and GEO-CAPE Airborne Simulator (GCAS) (Judd et al., 2020).

Additionally, to help identify and attribute air pollutants during highly polluted events in 2023 (Section 3.3), the Joint Polar Satellite System-1 Cross-track Infrared Sounder (JPSS-1/CrIS, with descending/ascending nodes of ~1:30/13:30 local time) O_3, carbon monoxide (CO), and PAN level 2 daily summary data provided by the TRopospheric Ozone and Precursors from Earth System Sounding project, were analyzed. The analysis of these extreme events was also supported by eight ozonesondes launched from the Virginia Commonwealth University Rice Rivers Center (RRC, 37.33197°N, 77.20842°W) during the inaugural edition of NASA Student airborne Research Program (SARP)-East campaign in summer 2023 along with model results and ground-based observations (Section 2.2.3).

2.2.2 Satellite SM and precipitation products

To characterize drought conditions and their temporal variability, which interact with atmospheric chemistry, NASA's L-band Soil Moisture Active Passive (SMAP) 9 km enhanced surface (first 5 cm belowground) SM (SSM) data version 5 were utilized, as well as the version 7 of daily precipitation data from the NASA-JAXA Global Precipitation Measurement (GPM) produced at 0.1°×0.1° resolution using the Integrated Multi-satellitE Retrievals for GPM-Final run algorithm. Despite the different sampling strategies and retrieval algorithms of SMAP and GPM, interannual variability in the drought conditions indicated by these SSM and precipitation data are qualitatively consistent (Fig. 4), which are also consistent with information from independent sources such as the North American Drought Monitor (https://www.ncei.noaa.gov/access/monitoring/nadm, last access: 22 December 2023). In addition to rainfall, irrigation water and other elements relevant to water and energy balances can also impact the variability in SSM which has feedback to the regional precipitation patterns. The wide range of SSM from <0.2 to >0.5 m^3 m^{-3} and its interannual differences which often exceed 0.1 m^3 m^{-3}, indicate the diverse SM regimes (i.e., dry, transitional, and wet) and therefore spatially and temporally varying land-atmosphere coupling strengths (Seneviratne et al., 2010, and references therein). The varying SSM-temperature coupling strengths were determined based on WRF-Chem results, with support of the 0.25°×0.25° European Centre for Medium-Range Weather Forecasts Reanalysis version 5 (ERA5) surface air temperature field. In a case study (Section 3.1), SMAP SSM data were assimilated into the Noah-MP LSM to improve the land ICs of WRF-Chem, and further, the modeled weather and atmospheric chemistry fields.

2.2.3 Ground-based observations

Hourly surface ultraviolet absorbance O_3 observations from the US EPA's Air Quality System (AQS, a major source of the TOAR database, last update in October 2023, and the record is more complete through part of July 2023) were used to support the quantification of O_3 temporal variability and model evaluation. AQS NO_2 measurements using the chemiluminescence detection with catalytic conversion, which are known to be positively biased by up to 50% due to NO_z (NO_y-NO_x) interferences (e.g., Dunlea et al., 2007), were also examined to help qualitatively understand surface NO_2 variability. AQS NO_2 data, available at much fewer urban/suburban areas, have poorer spatial coverage than their O_3 data. To support the interpretation and validation of results from the DA case study (Section 3.1), gauge-based precipitation

measurements and SSM measured using HydraProbe sensors at Harvard Forest, Massachusetts (42.53523°N, 72.17393°W) and a US Climate Reference Network (CRN) site in Millbrook, New York (41.786°N, 73.74°W) during the July 2022 SMAP validation experiment (SMAPVEX22) were utilized. While long-term direct chemical flux measurements are extremely limited, independently developed nitrogen deposition datasets, some of which integrated surface or/and satellite observations

245   with other models (e.g., Schwede and Lear, 2014; Fu et al., 2022; Rubin et al., 2023), will be referred to in the discussions.

2.3 Case studies and sensitivity simulations

Temporal variability of Nr and O_3 concentrations and fluxes at subregional-to-local scale are partially driven by hydrological variability which can be influenced by both precipitation and human activities such as irrigation. Two sets of modeling and DA case studies (Sections 2.3.1 and 2.3.2) were conducted to show that the modeled land surface states, such as SM, can be

250   improved via land DA and/or updating the model's irrigation schemes, which further impacts the modeled land-atmosphere exchange processes and atmospheric fields.

2.3.1 Effects of SM DA on modeled NO_2 and O_3

For this case study, SMAP morning-time (~6 am local time) SSM data were bias-corrected via matching the means and standard deviations of SMAP and Noah-MP SSM monthly climatology. The bias-corrected data were then assimilated into

255   the Noah-MP LSM using a 40-member ensemble Kalman filter approach to adjust WRF-Chem's land ICs during July 2018 and July 2022. Meteorological forcing (precipitation, short- and longwave radiation) and state (Noah-MP SM) perturbation attributes were set up largely based on Kumar et al. (2009) recommendations for the Noah LSM, and the input observation error standard deviation was set to be 0.04 $m^3 m^{-3}$ according to the SMAP data quality requirement. Through this experiment we evaluate whether and to what extent can satellite SM DA improve the day-to-day (i.e., before and after a precipitating

260   event during the SMAPVEX22 campaign when in-situ SSM data were also collected near the SMAP morning overpassing times) and interannual variability (i.e., July 2018 and July 2022) of Noah-MP SM, even in dense vegetation regions such as the eastern US where satellite SM retrieval is generally more challenging. How the adjustments to Noah-MP land surface states by DA impacted the modeled atmospheric fields was also quantified.

265   ### 2.3.2 Irrigation impacts on O_3 vegetation uptake and Nr deposition
Using flux-based O_3 metrics derived from model outputs, recent studies (Mills et al., 2018; Huang et al., 2022) estimated that the negative impacts of ground-level O_3 on crop yields are particularly large in humid irrigated and rainfed agricultural lands, where the plants' stomatal uptake of O_3 is significant. The global-scale coarse-resolution analysis for 2010–2012 by Mills et al. (2018), which was based on O_3-flux metrics, also estimated that irrigation promotes the O_3 impacts on wheat production

270   by up to ~10%. To dynamically evaluate in detail the irrigation impacts on land surface and atmospheric fields as well as the estimated O_3 and Nr ecosystem impacts across our study area for recent years, WRF-Chem sensitivity simulations were

conducted with three sets of irrigation configurations, defined as (a, b, c) below, and for each of these three scenarios, two simulations were conducted with and without O_3 vegetation impacts:

a) Full irrigation (baseline): Sprinkler irrigation occurs in the morning when rootzone SM drops below 50% of field capacity;

275 b) Reduced irrigation: Sprinkler irrigation occurs in the morning when rootzone SM drops below 25% of field capacity, and the estimated irrigation water usage for this scenario is ~1/6 of the full-irrigation scenario for irrigated areas south of ~37°N in our domain;

and c) Irrigation option was completely disabled.

This sensitivity analysis is focused on 21–30 June 2022, when irrigated fields in the Carolinas that grow mostly O_3-sensitive

280 wheat and cotton were under stress according to the Vegetation Drought Response Index produced by the National Drought Mitigation Center (Fig. S2). This region also encompasses Nr deposition hotpots that have been experiencing critical load exceedances (i.e., the amount of Nr deposition exceeds the critical load threshold, the point above which deposition could harm sensitive ecosystems). For this period, irrigation water consumption under the full-irrigation scenario may be higher than normal, and the estimated surface fluxes under reduced- and no-irrigation scenarios may be particularly smaller than

285 usual and more strongly constrained by SM.

2.3.3 Impacts of transboundary pollution on weather, air quality and ecosystems

The Northeast and Mid-Atlantic US air quality is regularly affected by pollutants emitted or/and formed in upwind US states and actions have been taken to tackle cross-state air pollution such as using the Cross-State Air Pollution Rule framework

290 (https://www.epa.gov/Cross-State-Air-Pollution/overview-cross-state-air-pollution-rule-csapr, last access: 12 January 2024). Periodically, distant sources including Canadian wildfires and O_3-rich stratospheric air also travel to the northeastern and Atlantic states. Satellite and in-situ observations are powerful in detecting such episodic events that occur more frequently in recent years, assisting with early warnings and early actions. To help quantify the impacts of such extreme events during 13–16 June 2023 on weather, air quality and ecosystems, a WRF-Chem sensitivity simulation with clean chemical BCs was

295 conducted and analyzed together with the baseline simulation and multiplatform observations.

3 Results and discussions

3.1 Nr emissions, concentrations, and deposition fluxes during 2018–2023

The modeled soil NO and HONO emissions vary strongly with SM as well as soil temperature that can be impacted by SM. Even without land DA the model fairly well reproduced the large-scale spatial gradients and interannual variability of SMAP

300 SSM (Figs. 4a and S3). Soil emissions exhibit notable monthly variations, with multi-year June- and July-mean values ~11% and ~59% higher than the May-mean, respectively, associated with overall warmer and drier conditions. These monthly variations, together with the ~8% and ~18% multiyear June-May and July-May mean differences in anth+fire emissions as well as modeled surface and column NO_2 fields, help interpret the higher AQS and TROPOMI NO_2 on warmer months over many rural areas, especially those near high-temperature agricultural regions (Fig. S4), a point Goldberg et al. (2021) also

305   highlighted. The maxima and minima of MJJ soil emissions are seen in 2022 and 2018, respectively, and the interannual variability of soil emissions roughly anti-correlates with that of SM with correlation coefficient r ranging from -0.63 to -0.40 (p<<0.01; Fig. 5a;c). For most years, the MJJ-mean soil NO and HONO emissions were particularly high in warm and/or dry areas including parts of the Carolinas, Virginia, New York, Michigan, and Canada's Ontario, where their contributions to the total soil+anth+fire NO_y emissions persistently exceeded 30% (Fig. 5a–b). Based on a global atmospheric chemistry model

310   with a similar soil emission scheme, previous estimates of soil NO emission contributions to column NO_2 for this area were rather minor compared to other US regions in 2005 (i.e., <15% uniformly, Vinken et al., 2014), when anth NO_x emissions were >25% higher than in 2018 according to the CAMS inventory and other estimates. Owing to the overall declining US anth emissions and the changing climate, soil emissions play an increasingly important role in controlling Nr, and further, O_3 air quality, in this area. Accordingly, the needs to properly parameterize soil emissions and accurately model soil

315   environments (e.g., SM, soil temperature, pH) have been growing stronger which could greatly benefit from laboratory and field experiments.

Despite the increasing anth NH_3 and fire Nr emission trends (Section 2.1) and the abovementioned interannual variability in soil NO and HONO emissions, total Nr, as well as surface NO_y emissions that contributed to >50% of the total Nr emissions

320   show decreasing year-to-year changes during 2018–2023 except for the dip in 2020 mainly attributable to the COVID lockdowns (Fig. 6a). Closely linked to such temporal changes in NO_y emissions, that in many areas overwhelm the effects of slower NO_2 and NO_y dry deposition (Fig. S5 and later discussions), the modeled column and surface NO_2 both display downward changes since 2018, with their lowest values occurring in 2020 (Figs. 6b and 7). From 2018 to 2023, on average, column and surface NO_2 dropped by 15–20%. Impacted by the decreasing NO_2, HCHO columns demonstrate much slower

325   year-to-year variations than NO_2 (Fig. S6) in large part because of the less significant NMVOC emission changes. Impacted mostly by shipping and lightning emissions as well as North American pollution outflows, the amount of NO_2 above the ocean is lower than overland. Early afternoon (near TROPOMI overpassing times) surface and column NO_2 are ~44% and ~29% lower than their daytime averages (13–24 UTC, roughly the sampling times of TEMPO and the anticipated GeoXO geostationary missions). The stronger subdaily variability in surface NO_2 than in column NO_2 reflects the impacts of

330   photochemistry and evolution of planetary boundary layer on the rapidly-changing vertical distributions of chemicals throughout the daytime which have also been demonstrated in Huang et al. (2017b) and other studies with aircraft observations. Dependent strongly on convection, lightning NO emissions vary strongly from year to year in terms of locations and magnitudes, having larger impacts on free-tropospheric and column-average NO_2 than surface NO_2 (Fig. S7). The column NO_2 spatiotemporal variability based on TROPOMI and WRF-Chem greatly resemble (Fig. 7a–b), and larger

335   model-TROPOMI discrepancies are seen over the areas possibly influenced by lightning NO emissions and transboundary pollution where both model and retrieval errors may be large. The interannual variations in such pollutant sources aloft may also explain the different interannual variability in surface and column NO_2 for some locations and years. AQS NO_2 data,

although sparsely distributed and positively biased, qualitatively confirmed the model-suggested year-to-year changes in surface NO_2 (Fig. S8).

340

Drought conditions, as well as the opposite directions of NO_y and NH_3 emission and concentration changes, helped shape the interannual variability in the total Nr deposition fluxes (Fig. 8a). Overland, the modeled Nr dry deposition fluxes often contributed to nearly or higher than 70% of the total Nr deposition. These contributions are larger than earlier estimates for this area: e.g., <60% in Tan et al., 2018, based on 11 global models, where wet deposition was stated to be overestimated.

345 This is likely due in part to known limitations in WRF-Chem wet deposition scheme that could lead to underestimated wet deposition (Ryu and Min, 2022). Another source of uncertainty may arise from the underestimation in modeled precipitation amount as well as the inaccuracy in modeled precipitation patterns referring to GPM on event-to-seasonal scales (Figs. 4b and S3 and Section 3.3.1 case study). This is a WRF behavior reported also in previous studies and could indirectly impact dry deposition modeling. Dry NO_y deposition fluxes decreased evidently (i.e., by 5–16% overall and >50% in some

350 populated areas) whereas NH_x dry deposition fluxes show up to ±3% of overall interannual variability and rose by >20% over certain agricultural lands (Fig. S9) where NH_3 emissions have been climbing up. Due to not applying a bi-directional approach (Zhang et al., 2010; Massad et al., 2010; Pleim et al., 2019), these NH_3 fluxes may be overestimated over source regions by a few percent (Zhu et al., 2015; Liu et al., 2020a). Nevertheless, the contrasting directions of change in NO_y and NH_x deposition fluxes as well as the importance of NH_x deposition in total deposition corroborate results from other studies

355 for earlier periods (e.g., Schwede and Lear, 2014; Li et al., 2015; Jia et al., 2016; Geddes and Martin, 2017; Liu et al., 2020b, and references therein). With merely several percent of interannual differences in flux partitioning (Fig. 8b–c), in all years' MJJ, HNO_3 and NH_3 contributions (>35%) dominated in the Nr dry deposition fluxes. NO dry deposition is negligible due to extremely high surface resistance and in figures is combined with NO_2 into NO_x fluxes, that contribute to 12–15% of Nr dry deposition fluxes. Unlike most other species, surface resistance of HNO_3 is nearly zero, whose dry deposition variability is

360 therefore driven dominantly by aerodynamic resistance and quasi-laminar sublayer resistance and responds differently to drought conditions than the other Nr species and O_3 (Section 3.2). The modeled HNO_3 daytime dry deposition velocities over most forested areas fall within 4–8 cm s^{-1}, close to the measurements reported in literature for similar land cover types in the eastern US (e.g., Nguyen et al., 2015). These are ~a factor of 10 higher than dry deposition velocities of NO_2 and PAN, similar to the results in Wu et al. (2011) based also on a photosynthesis-based dry deposition model and the flux

365 measurements summarized by Delaria and Cohen (2023).

Compared to global model estimated total and speciated Nr deposition fluxes for previous decades (e.g., Dentener et al., 2006; Paulot et al., 2018; Tan et al., 2018; Rubin et al., 2023), our regional model results present more details which could be beneficial for estimating critical load exceedances on smaller spatial scales. They are overall of a lower magnitude

370 reflecting the impacts of the declining NO_y and Nr emissions which are anticipated to continue into the coming decades. This may also be attributed to the impact of the changing climate and the model uncertainty relevant to scales, deficits in

deposition schemes and inputs as well as uncounted deposition of certain organic Nr species due to our chosen chemistry and aerosol schemes. Possibly also for these reasons, a little over 50% of the surface Nr emissions were estimated to be removed via deposition in this area for all years (Fig. 6a), slightly lower than the estimates in previous modeling studies. Comparing

375 our WRF-Chem Nr deposition fluxes to critical load thresholds in Simkin et al. (2016) that range from 7.4 to 19.6 kg ha^{-1} a^{-1}, during 2018–2023, the high likelihoods of critical load exceedances in Pennsylvania dropped whereas those for parts of North Carolina remained high. The Nr deposition fluxes stayed below these critical load thresholds over most of the northern forests, a region where primary productivity has been determined to be nitrogen-limited (Du et al., 2020) and can be highly sensitive to the interannual variability in Nr deposition.

380

3.2 Spatiotemporal variability of Nr and O$_3$ concentrations and deposition fluxes

The interannual, day-by-day and subdaily variability in HCHO/NO$_2$ ratios derived from TROPOMI and airborne GCAS and GeoTASO data manifests the variable photochemical environments driven by the changing meteorology and emissions, but, as noted in a number of prior studies (e.g., Duncan et al., 2010; Jin et al., 2017; Tao et al., 2022; Souri et al., 2023), can also

385 be affected by retrieval uncertainty and several other types of errors. Yet, they indicate that, much of the study area belong to NO$_x$-sensitive or transitional chemical regimes during 2018–2023 (i.e., HCHO/NO$_2$ higher than empirical thresholds of 2–4, Fig. 9) except very few megacities such as the Greater New York City and Toronto, Canada, and for those urban regions, O$_3$ formation continues the trends of turning sensitive to NO$_x$.

390 Largely explainable by the changing NO$_y$ emissions and NO$_x$-sensitive chemical regimes, the spatial patterns of the modeled interannual differences in column NO$_2$ and surface O$_3$ concentrations roughly resemble, both displaying downward changes over the majority of terrestrial areas whereas the opposite direction of changes over the Atlantic Ocean (Figs. 7b and 10a). Daytime surface O$_3$ concentrations exhibit more robust spatial correlations with early afternoon (19 UTC) NO$_2$ columns than HCHO columns, with correlation coefficient r of 0.54 and 0.40 for all years, respectively (Fig. 11). In more than half of the

395 terrestrial model grids, the interannual variability of 19 UTC NO$_2$ columns and daytime surface O$_3$ are moderately correlated (r>0.6), with the r value of 0.57 averaged across all overland grids and 0.92 for grids where the correlations are statistically significant (p<0.05). The reduction in NO$_y$ emissions contributed to the domain-average changes in median (-0.7 ppbv) and mean (-1.0 ppbv) daytime surface O$_3$ concentrations overland from 2018 to 2023 which are much smaller than that in 95th% O$_3$ (by -3.5 ppbv). The lowering NO$_y$ emissions also resulted in less titration, and consequently, the slightly increased 5th%

400 O$_3$ (by 0.3 ppbv). Such modeled general directions of O$_3$ temporal changes in this area over the past ~5 years are qualitatively consistent with Cooper et al. (2012) for springs and summers of 1990–2010 as well as follow-on studies (Simon et al., 2015; Lin et al., 2017; Gaudel et al., 2018). The interannual variability of imported O$_3$ and its precursors from other regions, as well as the interconnected environmental and plant physiological conditions (e.g., via soil-vegetation-atmosphere interactions whose strengths vary in space and time) modulated biogenic VOC emissions, deposition, chemical reactions,

405 transport and mixing, also drove the O$_3$ changes on regional-to-subregional scales.

The spatial patterns of WRF-Chem modeled surface O_3 broadly match the AQS observations for most of the years (Fig. 10), with root-mean-square errors (RMSEs) ranging from 4.1 to 6.5 ppbv which are significantly lower than the magnitudes of ~20 ppbv in many earlier modeling studies for the similar regions. The better performance may have substantially benefited

410   from the advancements in model parameterizations and the updated anth emission inputs. Although WRF-Chem surface and column NO_2 temporal changes agree well with the observed, the model struggled to capture the observed deviations of surface O_3 in 2023 from previous years (Fig. 10), likely due to its failure in representing the particularly strong influences of stratospheric O_3 or/and other extra-regional sources on the lower free tropospheric and surface O_3 in 2023 (Figs. 3b and S1). Later in a case study, the dependency of WRF-Chem O_3 performance on how well transboundary pollution as well as

415   regional climatic conditions and their driving processes are represented in the model will be investigated further.

Similar to dry deposition of Nr species and conclusions from Huang et al. (2022), the spatiotemporal variability of O_3 dry deposition velocities is closely linked with land cover types, environmental and vegetation conditions, with their highest daytime-average values ($v_{d,o3}$ >1.0 cm s^{-1}) seen over moist forests and >30% lower daytime-average values over croplands

420   experiencing drier conditions (Figs. S5 and S9). Cumulative stomatal O_3 uptake (CUO), a recommended metric for assessing the potential O_3 vegetation impact, that is affected by stomatal conductance, boundary layer resistance, and surface O_3 levels, appears also high over the croplands in Ohio and Indiana (~40 mmol m^{-2}) where surface O_3 concentrations are high while much lower over drier croplands in the Carolinas (<30 mmol m^{-2}). Except for regions influenced by the wetter-than-normal conditions or/and increasing surface O_3 concentrations, the CUO fields show declining trends (i.e., overall dropped by ~10%

425   from 2018 to 2023). Our results are qualitatively consistent with those in Clifton et al. (2020) for the northeastern US, where based on a global model, stomatal O_3 uptake cumulated through MJJ 2010 with no detoxification threshold was estimated to be ~35 mmol m^{-2}, and that flux was projected to decrease under the future climate. As indicated in Fig. 12a, the modeled CUO values are higher over croplands and forests than shrub/grass averagely and more spatially variable. The CUO fluxes display much clearer trends in most grids than the total Nr deposition fluxes, due to NO_y and NH_x deposition fluxes having

430   competing directions of changes through the past years. The potential impacts of Nr deposition are strongest and weakest on croplands and water, respectively (Fig. 12b).

3.3 Three case studies

3.1 Land DA

435   As indicated by GPM, SMAP, and in-situ observations collected at Harvard Forest and the CRN-Millbrook site during the SMAPVEX22 campaign, a precipitating event associated with a frontal passage occurred from late 13 July to early 14 July 2022 causing sharp increases in SSM around 14 July in Massachusetts (by >0.06 m^3 m^{-3}) and parts of the eastern New York (by ~0.02 m^3 m^{-3}) where surface O_3 dropped abruptly by up to 30 ppbv (Figs. 13a and S10). Baseline simulation without DA failed to reproduce this strong daily SSM variability at site-to-regional scales (Fig. 13b). After enabling the SMAP DA,

440 Noah-MP SSM in Massachusetts and the eastern New York increased remarkably on 14 July (Fig. 13c), better matching the observed quantities. Along the southern New York-Connecticut as well as the northern New York-Vermont borders, the slightly drier conditions on 14 July are also better represented in Noah-MP with the implementation of SMAP DA (Fig. 13a–c). The enhancements in soil wetness resulted in a bit cooler surface soil/air, thinner atmospheric boundary layer, suppressed biogenic VOC and soil NO_y emissions as well as O_3 formation while deposition accelerated. Lightning emissions were also

445 sensitive to the DA-induced SM changes. Consequently, above many Connecticut River watershed areas, WRF-Chem NO_2 columns dropped (Fig. 13e–f); and both enhancements and reductions in daytime surface O_3 levels (not shown in figures) are found due to increased upwind pollution contributions whereas weakened local emissions and production. Referring to ~50 AQS observations across the New England region (40.5–43°N, 70–74°W), for 14 July, WRF-Chem daytime surface O_3 mean bias and RMSE (~2.1 and ~5.4 ppbv, respectively) were reduced by the DA by ~0.5 and ~0.1 ppbv, respectively. It is

450 also highlighted that the various processes SM can impact help shape the vertical profiles of NO_2 and other chemical species, a critical ancillary data for calculating the air mass factor that is needed to convert slant columns to vertical columns in satellite retrievals (Lorente et al., 2017) and derive averaging kernels (AKs, Eskes and Boersma, 2003). At Harvard Forest, the vertical distributions of NO_2 as well as their responses to SMAP DA changed rapidly during this event (Fig. 13g–h), despite the minor change in NO_2 column. It is suggested that cautions are taken when attributing the mismatches between

455 TROPOMI and models (with AKs, that indicate lower TROPOMI sensitivity towards the surface) over the scenes where NO_x near the surface and aloft may both be significant. Also, productions, interpretations, and applications of satellite NO_2 retrievals could benefit from evaluating and tuning their model-based *a priori* profiles with in-situ measurements of NO_2 vertical distributions under various environments.

460 Figure 14a–c illustrates that, on a larger timescale, SMAP DA effectively narrowed the Noah-MP wet biases in July 2022-July 2018 SSM differences in Canada's Ontario (croplands) as well as the dry biases in Virginia (forests) that may have resulted from inaccurate representations of meteorological drought conditions. WRF-Chem weather fields, biogenic VOC, soil NO_y and lightning emissions, and deposition processes all responded to the DA-induced changes in the model's land ICs. The July 2022-July 2018 differences of WRF-Chem NO_2 columns and surface O_3 over these regions became closer to

465 (by up to ~50% and 4 ppbv, respectively) what TROPOMI and AQS observations indicate (Fig. 14d–i). Notably, the SMAP DA flipped the sign of surface O_3 interannual differences over the northern Virginia. The remaining modeled-observed NO_2 and O_3 discrepancies over some of the northern states and coastal North Carolina, which are highly correlated because of the dominating NO_x-limited regime, can also be explained by uncertainties in the model's chemical BCs and wind fields.

470 These analyses demonstrate that microwave satellite SM DA can improve the modeled SM dynamics at daily-to-interannual timescales. Similar findings were previously reported by Draper and Reichle (2015) where SM from the X-band (sensitive to top ~1 cm soil) Advanced Microwave Scanning Radiometer-Earth Observing System was assimilated at only four sites, but not on regional scales for forested regions where SM retrievals have been considered challenging and need validation. It is

also shown in this work that the DA adjustments to LSMs' SM fields can positively impact weather and chemistry fields
475 from their coupled atmospheric models, benefiting our interpretations and prediction skills of air pollutants' distributions and
temporal changes which can in turn help advance satellite retrievals. It is important to note that SSM-atmosphere coupling
strengths vary strongly in space and time, influenced by the evolution of local hydrological regimes. As 2022-2018 SSM and
surface air temperature differences show strong negative correlations of -0.78 (Fig. S11), the land DA impacts on WRF-
Chem's atmospheric chemistry fields were partially through adjusting the weather. For the times/locations that SSM and
480 atmosphere coupling strengths are weak, land DA is anticipated to impact the modeled atmospheric chemistry fields mostly
via the direct control of land surface on natural emissions and deposition.

3.2 Irrigation approaches

Based on the three sets of simulations representing full-, reduced-, and no-irrigation scenarios (Section 2.3.2), the impacts of
485 irrigation on surface O_3 concentrations, CUO and O_3 injury to vegetation, as well as Nr deposition were quantified (Fig. 15).
Ozone perturbs gross primary productivity more strongly (up to 20–30%) than transpiration (mostly <10%), and therefore
reduces the vegetation water use efficiency. Its reductions to leaf biomass over the stressed irrigated lands in the Carolinas in
late June 2022 are estimated to be <5% under all three scenarios. Under the limited- and no-irrigation conditions, O_3-induced
crop yield losses were reduced over irrigated areas by up to ~2%, a result of lowered SM (Fig. S12) and deposition fluxes
490 despite the enhanced soil/air temperatures, soil NO_y emissions and surface O_3 concentrations (by up to ~10 ppbv). This result
supports and extends the findings from previous coarse-resolution modeling (Mills et al., 2018) and observational (Harmens
et al., 2019) studies. The period-integrated O_3 stomatal uptake increased slightly outside of the irrigated land due to higher
O_3 being transported away from the irrigated areas. Over irrigated areas, the estimated total Nr deposition would also be
lower under reduced- and no-irrigation scenarios by more than 50%, which would be below possible critical load thresholds
495 (Simkin et al., 2016), as less irrigation would result in stronger atmospheric mixing and reduced SM although soil NO_y
emissions would increase. The impacts of irrigation on Nr deposition over non-irrigated areas are rather noisy and more
intense than on O_3, highlighting the complex net effects of irrigation-induced changes in land surface and meteorological
conditions on a group of species with substantially different properties undergoing various atmospheric processes.

500 Compared with long-term offline LSM simulations forced by independently produced O_3 data, evaluations of O_3 vegetation
impacts using coupled modeling systems like WRF-Chem with land surface feedback to regional weather and atmospheric
chemistry being accounted for are more realistic. Nevertheless, such approaches are hundreds of times more computationally
expensive and may be subject to uncertainty from the atmospheric model. Survey- and satellite-based irrigation types and
water use information, including wastewater use that may impact plant growth, nutrient supply and soil environments (Aman
505 et al., 2018), direct stationary and/or airborne measurements of water, carbon, energy, air pollutants' concentrations and
fluxes, as well as plant traits within and outside of irrigated areas for variable hydroclimatic conditions, would help evaluate

and improve irrigation modeling and the model-based holistic assessments of irrigation impacts on regional environments that could assist with forming pollution mitigation and ecosystem adaptation strategies for future.

3.3 Transboundary pollution

Periodically, distant pollution sources make strong environmental impacts on the Northeast and Mid-Atlantic US states. For example, during the 2023 SARP-East campaign, JPSS-1/CrIS observed high O_3 and low CO on 13 June; and high O_3, CO, and PAN on the following days of the same week (Fig. 16) when elevated NH_3 columns and aerosol optical depths were also observed from space by multiple instruments (not shown). These data suggest that long-range transported stratospheric air and Canadian wildfire plumes reached the eastern US.

As indicated by the stratospheric O_3 tracer of the chemical BC model WACCM, the 13 June stratospheric intrusion event associated with a frontal passage enhanced lower tropospheric O_3 by as high as 30–40 ppbv along the northeast corridor, which helps explain the spike at ~700 hPa (>30 ppbv O_3 enhancement) in the SARP-East RRC ozonesonde profile for that day (Fig. 17a–b). The estimated stratospheric impact on surface O_3 across the domain is only ¼–1/3 as large, consistent with prior knowledge that stratospheric impacts on the US East are often confined at higher altitudes while surface O_3 remains low (Ott et al., 2016). Thick Canadian wildfire plumes that moved into the study region, dramatically enhanced O_3 spanning a wide altitude range (i.e., from >900 hPa to ~600 hPa) above the RRC site on several days of that week (Fig. 17b). WRF-Chem moderately well reproduced the daytime surface O_3 patterns observed at AQS sites, with RMSEs of ~7 ppbv (Fig. 17c–f;g–j). Under th strong influences of Canadian fires, O_3 in the US outflows during that week was close to that in air sampled ~two decades ago along the East Coast (Cooper et al., 2005). Ozonesondes also indicate that air quality improved remarkably in the following week, with O_3 from the surface to ~700 hPa nearly 40 ppbv lower (Fig. 17b).

A WRF-Chem sensitivity simulation using clean chemical BCs was conducted and analyzed together with the baseline simulation during 13–16 June 2023. Extremely high transported background aerosols and their precursors due to Canadian wildfires along with upwind US pollution interacted with meteorological and land surface fields (e.g., radiation, temperature, clouds, precipitation, and surface wetness) that are relevant to evapotranspiration and photosynthesis (see also discussions on Asian anth pollution impacts in Huang et al., 2020, and references therein), dry/wet deposition velocity/coefficient and secondary pollutant formation. Although under the highly polluted conditions, overall dry deposition velocities (Fig. S13) are reduced and photochemistry activities are weakened, the period-integrated CUO and mean total Nr deposition fluxes are enhanced as the excessive amount of imported pollution significantly elevated surface O_3 and Nr concentrations (Fig. 18). During this period, daily O_3 stomatal uptake and the mean total Nr deposition overland are ~2% and ~26% higher than their 2023 seasonal-mean values, respectively. This sensitivity analysis not only supports the findings about fire emission impacts on deposition from offline air quality modeling studies (e.g., Koplitz et al., 2021), but also stresses the importance of accounting for aerosol radiative effects in assessing ecosystem impacts of pollutants from biomass burning and other sources.

Previous work has focused strongly on the impacts of long-range transport of pollution from Asia and the stratosphere on the western US O_3 trends (e.g., Cooper et al., 2012; Lin et al., 2017; Miyazaki et al., 2022). This case study demonstrates that extra-regional pollution can also compromise the efforts of improving air quality via controlling local and regional emissions

545 over the eastern US. Possibly linked to climate change, such highly polluted events occurred more frequently during the 2023 warm season (e.g., there were at least two other known extreme events in June 2023 due to Canadian wildfire impacts), exerting controls on surface-atmosphere exchange processes and perturbing the long-term changes in O_3, Nr and other chemical compounds. More accurate and consistently-configured chemical BC models or reanalysis products, preferably at higher resolutions with a more complete list of prognostic and diagnostic variables, are essential for further regional-scale

550 modeling investigations on such events and their contributions to trends/variability. Addition of stratospheric tracers and accurate, time-varying upper chemical boundary conditions to regional models, assisted with O_3 profile measurements from commercial aircraft, sondes, and Lidar networks, are expected to be also helpful for diagnosing and/or reducing errors in the simulations of some of such events.

4 Summary and suggested future directions

555 Based on WRF-Chem model simulations and multiplatform observations, this paper discussed Nr and O_3 concentrations and fluxes during 2018–2023 in the northeastern and mid-Atlantic US, most of which fell into NO_x-limited and transitional chemical regimes. Effective local emission controls resulted in evident decreases in NO_2 and surface O_3 concentrations, with the reduced human activities during COVID lockdowns also contributing to their low values in ~2020. Current polar-orbiting satellites take snapshots of NO_2 columns only at a particular time of day, such as in the early afternoon when surface NO_2

560 experienced their daily lows. With this sparse temporal sampling, TROPOMI did not miss the general NO_2 interannual and seasonal variability and filled in the extremely large horizontal gaps between surface AQS observations most of which are in/near urban regions and positively biased. Recently-launched and planned geostationary satellite missions such as TEMPO and GeoXO will be invaluable for refined analyses concerning the subdaily variability of NO_2 and other variables.

565 The declines in NO_y emissions and concentrations were roughly consistent with the temporal changes in NO_y deposition, which were balanced out by the overall rising agricultural and total NH_x emissions and deposition. The changes in NO_y and NH_x deposition together shaped the interannual variability in Nr deposition in contrast to the clearer downward trends in O_3 vegetation uptake that reduced plants' water use efficiency and caused biomass/crop yield losses by a few percent. Certain hotspots of Nr deposition in North Carolina may have continued to exceed the empirical critical load thresholds reported in

570 literature, while the productivity of northern forests was estimated to have become more nitrogen-limited. Integrating nitrogen dynamics into LSMs could help improve their performance on land surface states as well as carbon, water, and energy fluxes, and further, the representations of Nr and O_3 deposition processes and their interactions in coupled modeling systems. Standard versions of Noah-MP, including what was used in this work, represent nitrogen stress by applying

constant foliage nitrogen factors (<1) in maximum carboxylation rate calculations (Niu et al., 2011). Following the JULES
575 and Community Land Model, Cai et al. (2016) started to add nitrogen dynamics to Noah-MP. Running offline, their updated
model yielded more accurate net primary productivity and evapotranspiration, and that may also be embedded into Earth
system models in future, with the magnitudes and spatiotemporal variability of its Nr inputs (e.g., from deposition and
fertilizer applications) being improved with the aid of atmospheric chemistry model routines or/and observations.

580 With updated model parameterizations and anth emissions, the used WRF-Chem system performed stably and remarkably
better on eastern US surface O_3 than those in literature. This paper highlighted that, temporal variability of Nr and O_3
concentrations and fluxes on subregional-to-local scales were partially driven by hydrological variability that can be
influenced by precipitation and controllable human activities such as irrigation. Like deposition processes, biogenic soil Nr
and VOC emissions that are highly sensitive to various climatic factors and plants' physiological conditions, as well as extra-
585 regional sources (e.g., dense wildfire plumes from the western US and Canada, and O_3-rich stratospheric air), have been
playing increasingly important roles in controlling pollutants' budgets in this area as local emissions went down. It is worth
noting that, urban emissions and air pollutants can be transported to and deposited into rural and remote regions, which may
better be modeled at finer resolutions (e.g., urban scale at 1–4 km or street-to-building scales) with the urban landscapes and
human influences on urban vegetation and soil properties being more carefully handled. Finer model resolutions may also
590 allow more processes, such as convection, to be explicitly resolved, but would need accurate inputs and observational
constraints at similar resolutions. To better inform the designs of mitigation and adaptation strategies, it is highly
recommended to continue evaluating and improving the parameterizations and inputs relevant to various sources and
processes in seamlessly coupled multiscale Earth system models using laboratory and field experiments in combination with
satellite DA. Further improved Earth system model results are expected to in turn benefit remote sensing communities, for
595 example, via serving as the retrieval *a priori* profiles for different types of environments.

Code and data availability

NASA-Unified Weather Research and Forecasting model (https://nuwrf.gsfc.nasa.gov/software, last access: 6 February
2024) output of O_3 and other key variables will be shared via Zenodo with the final version of this manuscript. Remote
sensing and in-situ data sets can be downloaded from: https://doi.org/10.5067/4DQ54OUIJ9DL (O'Neill et al., 2021),
600 https://doi.org/10.5067/GPM/IMERGDF/DAY/07 (Huffman et al., 2023); https://doi.org/10.5067/MHH8R0UZ5BMJ
(Bowman, 2022a); https://doi.org/10.5067/JL1HT3NGEAW3 (Bowman, 2022b); https://doi.org/10.5067/6HTQB4F81S08
(Bowman, 2022c); https://www-air.larc.nasa.gov/cgi-bin/ArcView/listos (Janz, 2020); and
https://aqs.epa.gov/aqsweb/airdata/download_files.html (US EPA, 2023b, last access: 6 February 2024). Gridded TROPOMI
data have been submitted by Isabelle De Smedt to TOAR-II Tropospheric Ozone Precursors Focus Group repository.

605 **Author contributions**

Overall study design and paper writing: MH leading, all participated in reviewing and editing

Design, execution, or discussions of model simulations: MH, GRC, JHC, SVK, ABG

Satellite data production, validation, delivery, and analysis: KWB, IDS, AC, MHC, MH

Field campaign deployments and data analysis: AC, MHC, SJJ, RMS, AMT, NMF, RJS, JDB, ATJ, MH

610 **Competing interests**

The authors declare that they have no competing interests.

Acknowledgements

NASA SMAP, SMAPVEX22 and LDAS sponsored part of the work. A contribution was made to this work at the Jet Propulsion Laboratory, California Institute of Technology, under a contract with NASA. We acknowledge the excellent

615 leadership of TOAR-II Tropospheric Ozone Precursors and Deposition Focus Group leads. We thank Antonin Soulie and team for helping with the CAMS global anth emissions, and Kyle DeLong for participating in collecting SM data in Harvard Forest during SMAPVEX22 that are used in this study.

References

Aman, M. S., Jafari, M., Reihan, M. K., Motesharezadeh, B., and Zare, S.: Assessing the Effect of Industrial Wastewater on

620 Soil Properties and Physiological and Nutritional Responses of Robinia Pseudoacacia, Cercis Siliquastrum and Caesalpinia Gilliesii Seedlings, J. Environ. Manag., https://doi.org/10.1016/j.jenvman.2018.03.087, 217, 718–726, 2018.

Bowman, K. W.: TROPESS CrIS-JPSS1 L2 Ozone for Forward Stream Summary Product, Version 1, Greenbelt, MD, USA, Goddard Earth Sciences Data and Information Services Center (GES DISC) [data set], Greenbelt, Maryland, USA,

625 https://doi.org/10.5067/MHH8R0UZ5BMJ, 2022a.

Bowman, K. W.: TROPESS CrIS-JPSS1 L2 Carbon Monoxide for Forward Stream Summary Product, Version 1, Greenbelt, MD, USA, Goddard Earth Sciences Data and Information Services Center (GES DISC) [data set], Greenbelt, Maryland, USA, https://doi.org/10.5067/JL1HT3NGEAW3, 2022b.

630

Bowman, K. W.: TROPESS CrIS-JPSS1 L2 Peroxyacetyl Nitrate for Forward Stream Summary Product, Version 1, Greenbelt, MD, USA, Goddard Earth Sciences Data and Information Services Center (GES DISC) [data set], Greenbelt, Maryland, USA, https://doi.org/10.5067/6HTQB4F81S08, 2022c.

635   Cai, X., Yang, Z.-L., Fisher, J. B., Zhang, X., Barlage, M., and Chen, F.: Integration of nitrogen dynamics into the Noah-MP
land surface model v1.1 for climate and environmental predictions, Geosci. Model Dev., 9, 1–15,
https://doi.org/10.5194/gmd-9-1-2016, 2016.

Carlton, A. G., Pinder, R. W., Bhave, P. V., and Pouliot, G. A.: To What Extent Can Biogenic SOA be Controlled? Environ.
640   Sci. Technol., 44, 3376–3380, https://doi.org/10.1021/es903506b, 2010.

Chai, T., Carmichael, G. R., Tang, Y., Sandu, A., Hardesty, M., Pilewskie, P., Whitlow, S., Browell, E. V., Avery, M. A.,
Nédélec, P., Merrill, J. T., Thompson, A. M., and Williams, E.: Four-dimensional data assimilation experiments with
International Consortium for Atmospheric Research on Transport and Transformation ozone measurements, J. Geophys.
645   Res.,112, D12S15, https://doi.org/10.1029/2006JD007763, 2007.

Chai, T., Kim, H.-C., Lee, P., Tong, D., Pan, L., Tang, Y., Huang, J., McQueen, J., Tsidulko, M., and Stajner, I.: Evaluation
of the United States National Air Quality Forecast Capability experimental real-time predictions in 2010 using Air Quality
System ozone and NO_2 measurements, Geosci. Model Dev., 6, 1831–1850, https://doi.org/10.5194/gmd-6-1831-2013, 2013.
650
Clifton, O. E., Lombardozzi, D. L., Fiore, A. M., Paulot, F., and Horowitz, L. W.: Stomatal conductance influences
interannual variability and long-term changes in regional cumulative plant uptake of ozone, Environ. Res. Lett., 15, 114059,
https://doi.org/10.1088/1748-9326/abc3f1, 2020.

655   Colarco, P. R., Schoeberl, M. R., Doddridge, B. G., Marufu, L. T., Torres, O., and Welton, E. J.: Transport of smoke from
Canadian forest fires to the surface near Washington, D.C.: Injection height, entrainment, and optical properties, J. Geophys.
Res., 109, D06203, https://doi.org/10.1029/2003JD004248, 2004.

Cooper, O. R., Stohl, A., Eckhardt, S., Parrish, D. D., Oltmans, S. J., Johnson, B. J., Nédélec, P., Schmidlin, F. J.,
660   Newchurch, M. J., Kondo, Y., and Kita, K.: A springtime comparison of tropospheric ozone and transport pathways on the
east and west coasts of the United States, J. Geophys. Res., 110, D05S90, https://doi.org/10.1029/2004JD005183, 2005.

Cooper, O. R., Gao, R.-S., Tarasick, D., Leblanc, T., and Sweeney, C.: Long-term ozone trends at rural ozone monitoring
sites across the United States, 1990–2010, J. Geophys. Res.,117, D22307, https://doi.org/10.1029/2012JD018261, 2012.
665
Darmenov, A. and da Silva, A.: The Quick Fire Emissions Dataset (QFED): Documentation of versions 2.1, 2.2 and 2.4,
NASA Technical Report Series, Global Modeling and Data Assimilation, NASA TM-2015-104606/Volume 38, available at:
http://gmao.gsfc.nasa.gov/pubs/docs/Darmenov796.pdf (last access: 12 January 2023), 2015.

670 De Smedt, I., Pinardi, G., Vigouroux, C., Compernolle, S., Bais, A., Benavent, N., Boersma, F., Chan, K.-L., Donner, S., Eichmann, K.-U., Hedelt, P., Hendrick, F., Irie, H., Kumar, V., Lambert, J.-C., Langerock, B., Lerot, C., Liu, C., Loyola, D., Piters, A., Richter, A., Rivera Cárdenas, C., Romahn, F., Ryan, R. G., Sinha, V., Theys, N., Vlietinck, J., Wagner, T., Wang, T., Yu, H., and Van Roozendael, M.: Comparative assessment of TROPOMI and OMI formaldehyde observations and validation against MAX-DOAS network column measurements, Atmos. Chem. Phys., 21, 12561–12593,
675 https://doi.org/10.5194/acp-21-12561-2021, 2021.

Dentener, F., Drevet, J., Lamarque, J. F., Bey, I., Eickhout, B., Fiore, A. M., Hauglustaine, D., Horowitz, L. W., Krol, M., Kulshrestha, U. C., Lawrence, M., Galy-Lacaux, C., Rast, S., Shindell, D., Stevenson, D., Van Noije, T., Atherton, C., Bell, N., Bergman, D., Butler, T., Cofala, J., Collins, B., Doherty, R., Ellingsen, K., Galloway, J., Gauss, M., Montanaro, V.,
680 Müller, J. F., Pitari, G., Rodriguez, J., Sanderson, M., Solmon, F., Strahan, S., Schultz, M., Sudo, K., Szopa, S., and Wild, O.: Nitrogen and sulfur deposition on regional and global scales: A multimodel evaluation, Global Biogeochem. Cy., 20, B4003, https://doi.org/10.1029/2005GB002672, 2006.

Delaria, E. R. and Cohen, R. C.: Measurements of Atmosphere–Biosphere Exchange of Oxidized Nitrogen and Implications
685 for the Chemistry of Atmospheric NO_x, Acc. Chem. Res., 56, 1720–1730, https://doi.org/10.1021/acs.accounts.3c00090, 2023.

Dix, B., Francoeur, C., Li, M., Serrano-Calvo, R., Levelt, P. F., Veefkind, J. P., McDonald, B. C., and de Gouw, J.: Quantifying NO_x Emissions from U.S. Oil and Gas Production Regions Using TROPOMI NO_2, ACS Earth and Space
690 Chem., 6, 403–414, https://doi.org/10.1021/acsearthspacechem.1c00387, 2022.

Doumbia, T., Granier, C., Elguindi, N., Bouarar, I., Darras, S., Brasseur, G., Gaubert, B., Liu, Y., Shi, X., Stavrakou, T., Tilmes, S., Lacey, F., Deroubaix, A., and Wang, T.: Changes in global air pollutant emissions during the COVID-19 pandemic: a dataset for atmospheric modeling, Earth Syst. Sci. Data, 13, 4191–4206, https://doi.org/10.5194/essd-13-4191-
695 2021, 2021.

Draper, C. and Reichle, R.: The impact of near-surface soil moisture assimilation at subseasonal, seasonal, and inter-annual timescales, Hydrol. Earth Syst. Sci., 19, 4831–4844, https://doi.org/10.5194/hess-19-4831-2015, 2015.

700 Du, E., Terrer, C., Pellegrini, A.F.A., Ahlström, A., van Lissa, C. J., Zhao, X., Xia, N., Wu, X., and Jackson, R. B.: Global patterns of terrestrial nitrogen and phosphorus limitation, Nat. Geosci., 13, 221–226, https://doi.org/10.1038/s41561-019-0530-4, 2020.

Duncan, B. N., Yoshida, Y., Olson, J. R., Sillman, S., Martin, R. V., Lamsal, L., Hu, Y., Pickering, K. E., Retscher, C.,
705   Allen, D. J., and Crawford, J. H.: Application of OMI observations to a space-based indicator of NO$_x$ and VOC controls on
surface ozone formation, Atmos. Environ., 44, 2213–2223, https://doi.org/10.1016/j.atmosenv.2010.03.010, 2010.

Dunlea, E. J., Herndon, S. C., Nelson, D. D., Volkamer, R. M., San Martini, F., Sheehy, P. M., Zahniser, M. S., Shorter, J.
H., Wormhoudt, J. C., Lamb, B. K., Allwine, E. J., Gaffney, J. S., Marley, N. A., Grutter, M., Marquez, C., Blanco, S.,
710   Cardenas, B., Retama, A., Ramos Villegas, C. R., Kolb, C. E., Molina, L. T., and Molina, M. J.: Evaluation of nitrogen
dioxide chemiluminescence monitors in a polluted urban environment, Atmos. Chem. Phys., 7, 2691–2704,
https://doi.org/10.5194/acp-7-2691-2007, 2007.

Elguindi, N., Granier, C., Stavrakou, T., Darras, S., Bauwens, M., Cao, H., Chen, C., Denier van der Gon, H. A. C.,
715   Dubovik, O., Fu, T. M., Henze, D. K., Jiang, Z., Keita, S., Kuenen, J. J. P., Kurokawa, J., Liousse, C., Miyazaki, K., Müller,
J. F., Qu, Z., Solmon, F., and Zheng, B.: Intercomparison of Magnitudes and Trends in Anthropogenic Surface Emissions
From Bottom-Up Inventories, Top-Down Estimates, and Emission Scenarios, Earths Future, 8, e2020EF001520,
https://doi.org/10.1029/2020EF001520, 2020.

720   Emberson, L.: Effects of ozone on agriculture, forests and grasslands, Phil. Trans. R. Soc. A., 378, 20190327,
https://doi.org/10.1098/rsta.2019.0327, 2020.

Erisman, J. W., Van Pul, A., and Wyers, P.: Parameterization of surface resistance for the quantification of atmospheric
deposition of acidifying pollutants and ozone, Atmos. Environ., 28, 2595–2607, https://doi.org/10.1016/1352-
725   2310(94)90433-2, 1994.

Eskes, H. J. and Boersma, K. F.: Averaging kernels for DOAS total- column satellite retrievals, Atmos. Chem. Phys., 3,
1285–1291, https://doi.org/10.5194/acp-3-1285-2003, 2003.

730   Felzer, B. S., Cronin, T. W., Melillo, J. M., Kicklighter, D. W., and Schlosser, C. A.: Importance of carbon-nitrogen
interactions and ozone on ecosystem hydrology during the 21st century, J. Geophys. Res., 114, G01020,
https://doi.org/10.1029/2008JG000826, 2009.

Fiore, A. M., Dentener, F. J., Wild, O., Cuvelier, C., Schultz, M. G., Hess, P., Textor, C., Schulz, M., Doherty, R. M.,
735   Horowitz, L. W., MacKenzie, I. A., Sanderson, M. G., Shindell, D. T., Stevenson, D. S., Szopa, S., van Dingenen, R., Zeng,
G., Atherton, C., Bergmann, D., Bey, I., Carmichael, G., Collins, W. J., Duncan, B. N., Faluvegi, G., Folberth, G., Gauss,

M., Gong, S., Hauglustaine, D., Holloway, T., Isaksen, I. S. A., Jacob, D. J., Jonson, J. E., Kaminski, J. W., Keating, T. J., Lupu, A., Marmer, E., Montanaro, V., Park, R. J., Pitari, G., Pringle, K. J., Pyle, J. A., Schroeder, S., Vivanco, M. G., Wind, P., Wojcik, G., Wu, S., and Zuber, A.: Multimodel estimates of intercontinental source-receptor relationships for ozone pollution, J. Geophys. Res., 114, D04301, https://doi.org/10.1029/2008JD010816, 2009.

Fu, J. S., Carmichael, G. R., Dentener, F., Aas, W., Andersson, C., Barrie, L. A., Cole, A., Galy-Lacaux, C., Geddes, J., Itahashi, S., Kanakidou, M., Labrador, L., Paulot, F., Schwede, D., Tan, J., and Vet, R.: Improving Estimates of Sulfur, Nitrogen, and Ozone Total Deposition through Multi-Model and Measurement-Model Fusion Approaches, Environ. Sci. Technol., 56, 2134–2142, https://doi.org/10.1021/acs.est.1c05929, 2022.

Galloway, J. N., Aber, J. D., Erisman, J. W., Seitzinger, S. P., Howarth, R.W., Cowling, E. B., and Cosby, B. J.: The nitrogen cascade, Bioscience, 53, 341–356, https://doi.org/10.1641/0006-3568(2003)053[0341:TNC]2.0.CO;2, 2003.

Galloway, J. N., Dentener, F. J., Capone, D. G., Boyer, E. W., Howarth, R. W., Seitzinger, S. P., Asner, G. P., Cleveland, C. C., Green, P. A., Holland, E. A., Karl, D. M., Michaels, A. F., Porter, J. H., Townsend, A. R., and Vorosmarty, C. J.: Nitrogen cycles: past, present, and future, Biogeochemistry, 70, 153–226, https://doi.org/10.1007/s10533-004-0370-0, 2004.

Gaudel, A., Cooper, O. R., Ancellet, G., Barret, B., Boynard, A., Burrows, J. P., Clerbaux, C., Coheur, P. F., Cuesta, J., Cuevas, E., Doniki, S., Dufour, G., Ebojie, F., Foret, G., Garcia, O., Granados-Munoz, M. J., Hannigan, J. W., Hase, F., Hassler, B., Huang, G., Hurtmans, D., Jaffe, D., Jones, N., Kalabokas, P., Kerridge, B., Kulawik, S., Latter, B., Leblanc, T., Le Flochmoen, E., Lin, W., Liu, J., Liu, X., Mahieu, E., McClure-Begley, A., Neu, J. L., Osman, M., Palm, M., Petetin, H., Petropavlovskikh, I., Querel, R., Rahpoe, N., Rozanov, A., Schultz, M. G., Schwab, J., Siddans, R., Smale, D., Steinbacher, M., Tanimoto, H., Tarasick, D. W., Thouret, V., Thompson, A. M., Trickl, T., Weatherhead, E., Wespes, C., Worden, H. M., Vigouroux, C., Xu, X., Zeng, G., and Ziemke, J.: Tropospheric Ozone Assessment Report: Present-day distribution and trends of tropospheric ozone relevant to climate and global atmospheric chemistry model evaluation, Elementa-Sci. Anthrop., 6, 39, https://doi.org/10.1525/elementa.291, 2018.

Geddes, J. A. and Martin, R. V.: Global deposition of total reactive nitrogen oxides from 1996 to 2014 constrained with satellite observations of NO₂ columns, Atmos. Chem. Phys., 17, 10071–10091, https://doi.org/10.5194/acp-17-10071-2017, 2017.

Georgoulias, A. K., Boersma, K. F., van Vliet, J., Zhang, X., van der A, R., Zanis, P., and de Laat, J.: Detection of NO₂ pollution plumes from individual ships with the TROPOMI/S5P satellite sensor, Environ. Res. Lett., 15, 124037, https://doi.org/10.1088/1748-9326/abc445, 2020.

Goldberg, D. L., Anenberg, S. C., Kerr, G. H., Mohegh, A., Lu, Z., and Streets, D. G.: TROPOMI NO_2 in the United States: A detailed look at the annual averages, weekly cycles, effects of temperature, and correlation with surface NO_2 concentrations, Earth's Future, 9, e2020EF001665, https://doi.org/10.1029/2020EF001665, 2021.

775

Granier, C., S. Darras, H. Denier van der Gon, J. Doubalova, N. Elguindi, B. Galle, M. Gauss, M. Guevara, J.-P. Jalkanen, J. Kuenen, C. Liousse, B. Quack, D. Simpson, K. Sindelarova, The Copernicus Atmosphere Monitoring Service global and regional emissions, Copernicus Atmosphere Monitoring Service report, https://doi.org/10.24380/d0bn-kx16, 2019.

780 Griffin, D., McLinden, C. A., Dammers, E., Adams, C., Stockwell, C. E., Warneke, C., Bourgeois, I., Peischl, J., Ryerson, T. B., Zarzana, K. J., Rowe, J. P., Volkamer, R., Knote, C., Kille, N., Koenig, T. K., Lee, C. F., Rollins, D., Rickly, P. S., Chen, J., Fehr, L., Bourassa, A., Degenstein, D., Hayden, K., Mihele, C., Wren, S. N., Liggio, J., Akingunola, A., and Makar, P.: Biomass burning nitrogen dioxide emissions derived from space with TROPOMI: methodology and validation, Atmos. Meas. Tech., 14, 7929–7957, https://doi.org/10.5194/amt-14-7929-2021, 2021.

785

Harmens, H., Hayes, F., Sharps, K., Radbourne, A., and Mills, G.: Can Reduced Irrigation Mitigate Ozone Impacts on an Ozone-Sensitive African Wheat Variety? Plants, 8, 220, https://doi.org/10.3390/plants8070220, 2019.

Holt, J., Selin, N. E., and Solomon, S.: Changes in Inorganic Fine Particulate Matter Sensitivities to Precursors Due to
790 Large-Scale US Emissions Reductions, Environ. Sci. Technol., 49, 4834–4841, https://doi.org/10.1021/acs.est.5b00008, 2015.

Huang, M., Carmichael, G. R., Pierce, R. B., Jo, D. S., Park, R. J., Flemming, J., Emmons, L. K., Bowman, K. W., Henze, D. K., Davila, Y., Sudo, K., Jonson, J. E., Tronstad Lund, M., Janssens-Maenhout, G., Dentener, F. J., Keating, T. J., Oetjen,
795 H., and Payne, V. H.: Impact of intercontinental pollution transport on North American ozone air pollution: an HTAP phase 2 multi-model study, Atmos. Chem. Phys., 17, 5721–5750, https://doi.org/10.5194/acp-17-5721-2017, 2017a.

Huang, M., Carmichael, G. R., Crawford, J. H., Wisthaler, A., Zhan, X., Hain, C. R., Lee, P., and Guenther, A. B.: Biogenic isoprene emissions driven by regional weather predictions using different initialization methods: case studies during the
800 SEAC^{4}RS and DISCOVER-AQ airborne campaigns, Geosci. Model Dev., 10, 3085–3104, https://doi.org/10.5194/gmd-10-3085-2017, 2017b.

Huang, M., Crawford, J. H., Carmichael, G. R., Santanello, J. A., Kumar, S. V., Stauffer, R. M., Thompson, A. M., Weinheimer, A.J., and Park, J. D.: Impact of aerosols from urban and shipping emission sources on terrestrial carbon uptake

805 and evapotranspiration: A case study in east Asia, J. Geophys. Res. Atmos., 125, e2019JD030818, https://doi.org/10.1029/2019JD030818, 2020.

Huang, M., Crawford, J. H., DiGangi, J. P., Carmichael, G. R., Bowman, K. W., Kumar, S. V., and Zhan, X.: Satellite soil moisture data assimilation impacts on modeling weather variables and ozone in the southeastern US – Part 1: An overview,
810 Atmos. Chem. Phys., 21, 11013–11040, https://doi.org/10.5194/acp-21-11013-2021, 2021.

Huang, M., Crawford, J. H., Carmichael, G. R., Bowman, K. W., Kumar, S. V., and Sweeney, C.: Satellite soil moisture data assimilation impacts on modeling weather variables and ozone in the southeastern US – Part 2: Sensitivity to dry-deposition parameterizations, Atmos. Chem. Phys., 22, 7461–7487, https://doi.org/10.5194/acp-22-7461-2022, 2022.
815

Hudman, R. C., Moore, N. E., Mebust, A. K., Martin, R. V., Russell, A. R., Valin, L. C., and Cohen, R. C.: Steps towards a mechanistic model of global soil nitric oxide emissions: implementation and space based-constraints, Atmos. Chem. Phys., 12, 7779–7795, https://doi.org/10.5194/acp-12-7779-2012, 2012.

820 Huffman, G. J., Stocker, E. F., Bolvin, D. T., Nelkin, E. J., and Tan, J.: GPM IMERG Final Precipitation L3 1 day 0.1 degree ×0.1 degree, Version 7, Goddard Earth Sciences Data and Information Services Center (GES DISC) [data set], Greenbelt, Maryland, USA, https://doi.org/10.5067/GPM/IMERGDF/DAY/07, 2023.

Janz, S.: Long Island Sound Tropospheric Ozone Study GCAS and GeoTASO measurements of NO_2 and CH_2O, Version R1,
825 NASA Langley Research Center Airborne Science Data for Atmospheric Composition [data set], Hampton, Virginia, USA, available at: https://www-air.larc.nasa.gov/missions/listos/index.html (last access: 6 February 2024), 2020.

Jia, Y., Yu, G., Gao, Y., He, N., Wang, Q., Jiao, C., and Zuo, Y.: Global inorganic nitrogen dry deposition inferred from ground- and space-based measurements, Sci. Rep., 6, 19810, https://doi.org/10.1038/srep19810, 2016.
830

Jiang, X., Guenther, A., Potosnak, M., Geron, C., Seco, R., Karl, T., Kim, S., Gu, L., and Pallardy, S.: Isoprene emission response to drought and the impact on global atmospheric chemistry, Atmos. Environ., 183, 69–83, https://doi.org/10.1016/j.atmosenv.2018.01.026, 2018.

835 Jin, X., Fiore, A. M., Murray, L. T., Valin, L. C., Lamsal, L. N., Duncan, B., Boersma, K. F., De Smedt, I., Abad, G. G., Chance, K., and Tonnesen, G. S.: Evaluating a Space-Based Indicator of Surface Ozone-NO_x-VOC Sensitivity Over Midlatitude Source Regions and Application to Decadal Trends, J. Geophys. Res.-Atmos., 122, 10439–10461, https://doi.org/10.1002/2017JD026720, 2017.

840 Judd, L. M., Al-Saadi, J. A., Szykman, J. J., Valin, L. C., Janz, S. J., Kowalewski, M. G., Eskes, H. J., Veefkind, J. P., Cede, A., Mueller, M., Gebetsberger, M., Swap, R., Pierce, R. B., Nowlan, C. R., Abad, G. G., Nehrir, A., and Williams, D.: Evaluating Sentinel-5P TROPOMI tropospheric NO_2 column densities with airborne and Pandora spectrometers near New York City and Long Island Sound, Atmos. Meas. Tech., 13, 6113–6140, https://doi.org/10.5194/amt-13-6113-2020, 2020.

845 Koplitz, S. N., Nolte, C. G., Sabo, R. D., Clark, C. M., Horn, K. J., Thomas, R. Q., and Newcomer-Johnson, T. A.: The contribution of wildland fire emissions to deposition in the US: Implications for tree growth and survival in the Northwest, Environ. Res. Lett., 16, 024028, https://doi.org/10.1088/1748-9326/abd26e, 2021.

Koplitz, S., Simon, H., Henderson, B., Liljegren, J., Tonnesen, G., Whitehill, A., and Wells, B.: Changes in Ozone Chemical
850 Sensitivity in the United States from 2007 to 2016, ACS Environ. Au, 2, 206–222, https://doi.org/10.1021/acsenvironau.1c00029, 2022.

Kumar, S. V., Reichle, R. H., Koster, R. D., Crow, W. T., and Peters-Lidard, C. D.: Role of subsurface physics in the assimilation of surface soil moisture observations, J. Hydrometeorol., 10, 1534–1547,
855 https://doi.org/10.1175/2009JHM1134.1, 2009.

Lapina, K., Henze, D. K., Milford, J. B., Huang, M., Lin, M., Fiore, A. M., Carmichael, G., Pfister, G. G., and Bowman, K.: Assessment of source contributions to seasonal vegetative exposure to ozone in the U.S., J. Geophys. Res.-Atmos., 119, 324–340, https://doi.org/10.1002/2013JD020905, 2014.
860
Li, C., Martin, R. V., Cohen, R. C., Bindle, L., Zhang, D., Chatterjee, D., Weng, H., and Lin, J.: Variable effects of spatial resolution on modeling of nitrogen oxides, Atmos. Chem. Phys., 23, 3031–3049, https://doi.org/10.5194/acp-23-3031-2023, 2023.

865 Li, J., Mahalov, A., and Hyde, P.: Simulating the impacts of chronic ozone exposure on plant conductance and photosynthesis, and on the regional hydroclimate using WRF/Chem, Environ. Res. Lett., 11, 114017, https://doi.org/10.1088/1748-9326/11/11/114017, 2016.

Li, Y., Schichtel, B. A., Walker, J. T., Schwede, D. B., Chen, X., Lehmann, C. M. B., Puchalski, M. A., Gay, D. A., and
870 Collett Jr., J. L.: Increasing importance of deposition of reduced nitrogen in the United States, Proc. Natl. Acad. Sci. USA, 113, 5874–5879, https://doi.org/10.1073/pnas.1525736113, 2016.

Lin, M., Horowitz, L. W., Payton, R., Fiore, A. M., and Tonnesen, G.: US surface ozone trends and extremes from 1980 to 2014: quantifying the roles of rising Asian emissions, domestic controls, wildfires, and climate, Atmos. Chem. Phys., 17, 2943–2970, https://doi.org/10.5194/acp-17-2943-2017, 2017.

Liu, L., Zhang, X., Xu, W., Liu, X., Wei, J., Wang, Z., and Yang, Y.: Global estimates of dry ammonia deposition inferred from space-measurements, Sci. Total Environ., 730, 139189, https://doi.org/10.1016/j.scitotenv.2020.139189, 2020a.

Liu, L., Zhang, X., Xu, W., Liu, X., Lu, X., Wei, J., Li, Y., Yang, Y., Wang, Z., and Wong, A. Y. H.: Reviewing global estimates of surface reactive nitrogen concentration and deposition using satellite retrievals, Atmos. Chem. Phys., 20, 8641–8658, https://doi.org/10.5194/acp-20-8641-2020, 2020b.

Liu, J., Clark, L. P., Bechle, M., Hajat, A., Kim, S.-Y., Robinson, A., Sheppard, Lianne, Szpiro, A. A., and Marshall, J. D.: Disparities in air pollution exposure in the United States by race-ethnicity and income, 1990–2010, Environ. Health Perspect., 129, 127005, https://doi.org/10.1289/EHP8584, 2021.

Lombardozzi, D., Levis, S., Bonan, G., Hess, P. G., and Sparks, J. P.: The Influence of Chronic Ozone Exposure on Global Carbon and Water Cycles, J. Climate, 28, 292–305, https://doi.org/10.1175/JCLI-D-14-00223.1, 2015.

Lorente, A., Boersma, K. F., Yu, H., Dörner, S., Hilboll, A., Richter, A., Liu, M., Lamsal, L. N., Barkley, M., De Smedt, I., Van Roozendael, M., Wang, Y., Wagner, T., Beirle, S., Lin, J.-T., Krotkov, N., Stammes, P., Wang, P., Eskes, H. J., and Krol, M.: Structural uncertainty in air mass factor calculation for NO_2 and HCHO satellite retrievals, Atmos. Meas. Tech., 10, 759–782, https://doi.org/10.5194/amt-10-759-2017, 2017.

Massad, R.-S., Nemitz, E., and Sutton, M. A.: Review and parameterisation of bi-directional ammonia exchange between vegetation and the atmosphere, Atmos. Chem. Phys., 10, 10359–10386, https://doi.org/10.5194/acp-10-10359-2010, 2010.

Mills, G., Sharps, K., Simpson, D., Pleijel, H., Broberg, M., Uddling, J., Jaramillo, F., Davies, W. J., Dentener, F., van den Berg, M., Agrawal, M., Agrawal, S. B., Ainsworth, E. A., Buker, P., Emberson, L., Feng, Z., Harmens, H., Hayes, F., Kopbayashi, K., Paoletti, E., and Van Dingenen, R.: Ozone pollution will compromise efforts to increase global wheat production, Global Change Biol., 24, 3560–3574, https://doi.org/10.1111/gcb.14157, 2018.

Miyazaki, K., Neu, J. L., Osterman, G., and Bowman, K.: Changes in US background ozone associated with the 2011 turnaround in Chinese NO_x emissions, Environ. Res. Commun., 4, 045003, https://doi.org/10.1088/2515-7620/ac619b, 2022.

Monfreda, C., Ramankutty, N., and Foley, J. A.: Farming the planet: 2. Geographic distribution of crop areas, yields, physiological types, and net primary production in the year 2000, Global Biogeochem. Cycles, 22, GB1022, https://doi.org/10.1029/2007GB002947, 2008.

910

Monks, P. S., Ravishankara, A. R., von Schneidemesser, E., and Sommariva, R.: Opinion: Papers that shaped tropospheric chemistry, Atmos. Chem. Phys., 21, 12909–12948, https://doi.org/10.5194/acp-21-12909-2021, 2021.

Nguyen, T. B., Crounse, J. D., Teng, A. P., Clair, J. M. S., Paulot, F., Wolfe, G. M., and Wennberg, P. O.: Rapid deposition

915   of oxidized biogenic compounds to a temperate forest, Proc. Natl. Acad. Sci. USA, 112, E392–E401, https://doi.org/10.1073/pnas.1418702112, 2015.

Niu, G. Y., Yang, Z. L., Mitchell, K. E., Chen, F., Ek, M. B., Barlage, M., Kumar, A., Manning, K., Niyogi, D., Rosero, E., Tewari, M., and Xia, Y.: The community Noah land surface model with multiparameterization options (Noah-MP): 1. Model

920   description and evaluation with local-scale measurements, J. Geophys. Res.-Atmos., 116, D12109, https://doi.org/10.1029/2010JD015139, 2011.

O'Neill, P. E., Chan, S., Njoku, E. G., Jackson, T., Bindlish, R., Chaubell, J., and Colliander, A.: SMAP Enhanced L3 Radiometer Global and Polar Grid Daily 9 km EASE-Grid Soil Moisture, Version 5, NASA National Snow and Ice Data

925   Center Distributed Active Archive Center [data set], Boulder, Colorado, USA, https://doi.org/10.5067/4DQ54OUIJ9DL, 2021.

Oswald, R., Behrendt, T., Ermel, M., Wu, D., Su, H., Cheng, Y., Breuninger, C., Moravek, A., Mougin, E., Delon, C., Loubet, B., Pommerening-Röser, A., Sörgel, M., Pöschl, U., Hoffmann, T., Andreae, M. O., Meixner, F. X., and Trebs, I.:

930   HONO emissions from soil bacteria as a major source of atmospheric reactive nitrogen, Science, 341, 1233–1235, https://doi.org/10.1126/science.1242266, 2013.

Ott, L. E., Duncan, B. N., Thompson, A. M., Diskin, G., Fasnacht, Z., Langford, A. O., Lin, M., Molod, A. M., Nielsen, J. E., Pusede, S. E., Wargan, K., Weinheimer, A. J., and Yoshida, Y.: Frequency and impact of summertime stratospheric

935   intrusions over Maryland during DISCOVER-AQ (2011): New evidence from NASA's GEOS-5 simulations, J. Geophys. Res.-Atmos., 121, 3687–3706, https://doi.org/10.1002/2015JD024052, 2016.

Pleim, J. E., Ran, L., Appel, W., Shephard, M. W., and Cady-Pereira, K.: New bidirectional ammonia flux model in an air quality model coupled with an agricultural model, J. Adv. Model. Earth Syst., 11, 2934–2957,

940   https://doi.org/10.1029/2019MS0017282934, 2019.

Rasool, Q. Z., Bash, J. O., and Cohan, D. S.: Mechanistic representation of soil nitrogen emissions in the Community Multiscale Air Quality (CMAQ) model v5.1, Geosci. Model Dev., 12, 849–878, https://doi.org/10.5194/gmd-12-849-2019, 2019.

945

Rogers, H. M., Ditto, J. C., and Gentner, D. R.: Evidence for impacts on surface-level air quality in the northeastern US from long-distance transport of smoke from North American fires during the Long Island Sound Tropospheric Ozone Study (LISTOS) 2018, Atmos. Chem. Phys., 20, 671–682, https://doi.org/10.5194/acp-20-671-2020, 2020.

950   Rubin, H. J., Fu, J. S., Dentener, F., Li, R., Huang, K., and Fu, H.: Global nitrogen and sulfur deposition mapping using a measurement–model fusion approach, Atmos. Chem. Phys., 23, 7091–7102, https://doi.org/10.5194/acp-23-7091-2023, 2023.

Ryu, Y.-H. and Min, S.-K.: Improving wet and dry deposition of aerosols in WRF-Chem: Updates to below-cloud
955   scavenging and coarse-particle dry deposition, J. Adv. Model. Earth Syst., 14, e2021MS002792. https://doi.org/10.1029/2021MS002792, 2022.

Paulot, F., Jacob, D. J., and Henze, D. K.: Sources and Processes Contributing to Nitrogen Deposition: An Adjoint Model Analysis Applied to Biodiversity Hotspots Worldwide, Environ. Sci. Technol., 47, 3226–3233,
960   https://doi.org/10.1021/es3027727, 2013.

Paulot, F., Malyshev, S., Nguyen, T., Crounse, J. D., Shevliakova, E., and Horowitz, L. W.: Representing sub-grid scale variations in nitrogen deposition associated with land use in a global Earth system model: implications for present and future nitrogen deposition fluxes over North America, Atmos. Chem. Phys., 18, 17963–17978, https://doi.org/10.5194/acp-18-
965   17963-2018, 2018.

Sadiq, M., Tai, A. P. K., Lombardozzi, D., and Val Martin, M.: Effects of ozone–vegetation coupling on surface ozone air quality via biogeochemical and meteorological feedbacks, Atmos. Chem. Phys., 17, 3055–3066, https://doi.org/10.5194/acp-17-3055-2017, 2017.

970

Salmon, J. M., Friedl, M. A., Frolking, S., Wisser, D., and Douglas, E. M.: Global rain-fed, irrigated, and paddy croplands: A new high resolution map derived from remote sensing, crop inventories and climate data, Int. J. Appl. Earth Obs., 38, 321–334, https://doi.org/10.1016/j.jag.2015.01.014, 2015.

975   Schwede, D. B. and Lear, G. G.: A novel hybrid approach for estimating total deposition in the United States, Atmos. Environ., 92, 207-220, http://dx.doi.org/10.1016/j.atmosenv.2014.04.008, 2014.

Seinfeld, J. H. and Pandis, S. N.: Atmospheric chemistry and physics: from air pollution to climate change, Third edition, John Wiley & Sons, Inc., Hoboken, New Jersey, 2016.

980

Seneviratne, S. I., Corti, T., Davin, E. L., Hirschi, M., Jaeger, E. B., Lehner, I., Orlowsky, B., and Teuling, A. J.: Investigating soil moisture-climate interactions in a changing climate: A review, Earth-Sci. Rev., 99, 125–161, https://doi.org/10.1016/j.earscirev.2010.02.004, 2010.

985   Simkin, S. M., Allen, E. B., Bowman, W. D., Clark, C. M., Belnap, J., Brooks, M. L., Cade, B. S., Collins, S. L., Geiser, L. H., Gilliam, F. S., Jovan, S. E., Pardo, L. H., Schulz, B. K., Stevens, C. J., Suding, K. N., Throop, H. L., and Waller, D. M.: Conditional vulnerability of plant diversity to atmospheric nitrogen deposition across the United States, Proc. Natl. Acad. Sci. USA, 113, 4086–4091, https://doi.org/10.1073/pnas.1515241113, 2016.

990   Simon, H., Reff, A., Wells, B., Xing, J., and Frank, N.: Ozone Trends Across the United States over a Period of Decreasing NO_x and VOC Emissions, Environ. Sci. Technol., 49, 186–195, https://doi.org/10.1021/es504514z, 2015.

Simpson, D., Arneth, A., Mills, G., Solberg, S., and Uddling, J.: Ozone—the persistent menace: interactions with the N cycle and climate change, Curr. Opinion Environ. Sustain., 919, 9–10, https://doi.org/10.1016/j.cosust.2014.07.008, 2014.

995

Simpson, D. and Darras, S.: Global soil NO emissions for Atmospheric Chemical Transport Modelling: CAMS-GLOB-SOIL v2.2, Earth Syst. Sci. Data Discuss. [preprint], https://doi.org/10.5194/essd-2021-221, 2021.

Soulie, A., Granier, C., Darras, S., Zilbermann, N., Doumbia, T., Guevara, M., Jalkanen, J.-P., Keita, S., Liousse, C., Crippa,
1000   M., Guizzardi, D., Hoesly, R., and Smith, S.: Global Anthropogenic Emissions (CAMS-GLOB-ANT) for the Copernicus Atmosphere Monitoring Service Simulations of Air Quality Forecasts and Reanalyses, Earth Syst. Sci. Data Discuss. [preprint], https://doi.org/10.5194/essd-2023-306, in review, 2023.

Souri, A. H., Johnson, M. S., Wolfe, G. M., Crawford, J. H., Fried, A., Wisthaler, A., Brune, W. H., Blake, D. R.,
1005   Weinheimer, A. J., Verhoelst, T., Compernolle, S., Pinardi, G., Vigouroux, C., Langerock, B., Choi, S., Lamsal, L., Zhu, L., Sun, S., Cohen, R. C., Min, K.-E., Cho, C., Philip, S., Liu, X., and Chance, K.: Characterization of errors in satellite-based $HCHO/NO_2$ tropospheric column ratios with respect to chemistry, column-to-PBL translation, spatial representation, and retrieval uncertainties, Atmos. Chem. Phys., 23, 1963–1986, https://doi.org/10.5194/acp-23-1963-2023, 2023.

1010   Steinkamp, J. and Lawrence, M. G.: Improvement and evaluation of simulated global biogenic soil NO emissions in an AC-GCM, Atmos. Chem. Phys., 11, 6063–6082, https://doi.org/10.5194/acp-11-6063-2011, 2011.

Tao, M., Fiore, A. M., Jin, X., Schiferl, L. D., Commane, R., Judd, L. M., Janz, S., Sullivan, J. T., Miller, P. J., Karambelas, A., Davis, S., Tzortziou, M., Valin, L., Whitehill, A., Civerolo, K., and Tian, Y.: Investigating Changes in Ozone Formation
1015   Chemistry during Summertime Pollution Events over the Northeastern United States, Environ. Sci. Technol., 56, 15312–15327, https://doi.org/10.1021/acs.est.2c02972, 2022.

Tan, J., Fu, J. S., Dentener, F., Sun, J., Emmons, L., Tilmes, S., Sudo, K., Flemming, J., Jonson, J. E., Gravel, S., Bian, H., Davila, Y., Henze, D. K., Lund, M. T., Kucsera, T., Takemura, T., and Keating, T.: Multi-model study of HTAP II on sulfur
1020   and nitrogen deposition, Atmos. Chem. Phys., 18, 6847–6866, https://doi.org/10.5194/acp-18-6847-2018, 2018.

United Nations Economic Commission for Europe: Guidance documents and other methodological materials for the implementation of the 1999 Protocol to Abate Acidification, Eutrophication and Ground-level Ozone (Gothenburg Protocol), https://unece.org/gothenburg-protocol (last access: 12 January 2023), 1999.

1025

US Environmental Protection Agency (EPA): Nonattainment Areas for Criteria Pollutants (Green Book), https://www.epa.gov/green-book, 2023a.

US EPA: AQS Hourly Ozone Data, US EPA Office of Air Quality Planning and Standards/Outreach and Information
1030   Division/National Air Data Group [data set], Research Triangle Park, North Carolina, USA, available at: https://aqs.epa.gov/aqsweb/airdata/download_files.html (last access: 6 February 2024), 2023b.

US Global Change Research Program: Fifth National Climate Assessment, Crimmins, A. R., Avery, C. W., Easterling, D. R., Kunkel, K. E., Stewart, B. C., and Maycock, T. K. Eds., US. Global Change Research Program, Washington, DC, USA,
1035   https://doi.org/10.7930/NCA5.2023, 2023.

van der Velde, I. R., van der Werf, G. R., Houweling, S., Eskes, H. J., Veefkind, J. P., Borsdorff, T., and Aben, I.: Biomass burning combustion efficiency observed from space using measurements of CO and NO_2 by the TROPOspheric Monitoring Instrument (TROPOMI), Atmos. Chem. Phys., 21, 597–616, https://doi.org/10.5194/acp-21-597-2021, 2021.
1040

Vinken, G. C. M., Boersma, K. F., Maasakkers, J. D., Adon, M., and Martin, R. V.: Worldwide biogenic soil NO$_x$ emissions inferred from OMI NO$_2$ observations, Atmos. Chem. Phys., 14, 10363–10381, https://doi.org/10.5194/acp-14-10363-2014, 2014.

1045   Walker, J. T., Beachley, G., Amos, H. M., Baron, J. S., Bash, J., Baumgardner, R., Bell, M. D., Benedict, K. B., Chen, X., Clow, D. W., Cole, A., Coughlin, J. G., Cruz, K., Daly, R. W., Decina, S. M., Elliott, E. M., Fenn, M. E., Ganzeveld, L., Gebhart, K., Isil, S. S., Kerschner, B. M., Larson, R. S., Lavery, T., Lear, G. G., Macy, T., Mast, M. A., Mishoe, K., Morris, K. H., Padgett, P. E., Pouyat, R. V., Puchalski, M., Pye, H., Rea, A. W., Rhodes, M. F., Rogers, C. M., Saylor, R., Scheffe, R., Schichtel, B. A., Schwede, D. B., Sexstone, G. A., Sive, B. C., Sosa, R., Templer, P. H., Thompson, T., Tong, D.,

1050   Wetherbee, G. A., Whitlow, T. H., Wu, Z., Yu, Z., and Zhang, L.: Toward the improvement of total nitrogen deposition budgets in the United States, Sci. Total Environ., 691, 1328–1352, https://doi.org/10.1016/j.scitotenv.2019.07.058, 2019.

Wang, Y., Ge, C., Garcia, L. C., Jenerette, G. D., Oikawa, P. Y., and Wang, J.: Improved modelling of soil NO$_x$ emissions in a high temperature agricultural region: role of background emissions on NO$_2$ trend over the US, Environ. Res. Lett., 16,

1055   084061, https://doi.org/10.1088/1748-9326/ac16a3, 2021.

Wiedinmyer, C., Kimura, Y., McDonald-Buller, E. C., Emmons, L. K., Buchholz, R. R., Tang, W., Seto, K., Joseph, M. B., Barsanti, K. C., Carlton, A. G., and Yokelson, R.: The Fire Inventory from NCAR version 2.5: an updated global fire emissions model for climate and chemistry applications, Geosci. Model Dev., 16, 3873–3891, https://doi.org/10.5194/gmd-

1060   16-3873-2023, 2023.

Wong, J., Barth, M. C., and Noone, D.: Evaluating a lightning parameterization based on cloud-top height for mesoscale numerical model simulations, Geosci. Model Dev., 6, 429–443, https://doi.org/10.5194/gmd-6-429-2013, 2013.

1065   Wu, Z., Wang, X., Chen, F., Turnipseed, A. A., Guenther, A. B., Niyogi, D., Charusombat, U., Xia, B., Munger, J. W., and Alapaty, K.: Evaluating the calculated dry deposition velocities of reactive nitrogen oxides and ozone from two community models over a temperate deciduous forest, Atmos. Environ., 45, 2663–2674, https://doi.org/10.1016/j.atmosenv.2011.02.063, 2011.

1070   Zhang, L., Wright, L. P., and Asman, W. A. H.: Bi-directional air-surface exchange of atmospheric ammonia: A review of measurements and a development of a big-leaf model for applications in regional-scale air-quality models, J. Geophys. Res., 115, D20310, https://doi.org/10.1029/2009JD013589, 2010.

Zhu, L., Henze, D., Bash, J., Jeong, G.-R., Cady-Pereira, K., Shephard, M., Luo, M., Paulot, F., and Capps, S.: Global
1075 evaluation of ammonia bidirectional exchange and livestock diurnal variation schemes, Atmos. Chem. Phys., 15, 12823–
12843, https://doi.org/10.5194/acp-15-12823-2015, 2015.

Zhu, J. and Liang, X.-Z.: Impacts of the Bermuda High on regional climate and ozone over the United States, J. Climate, 26,
1018–1032, https://doi.org/10.1175/JCLI-D-12-00168.1, 2013.

1080
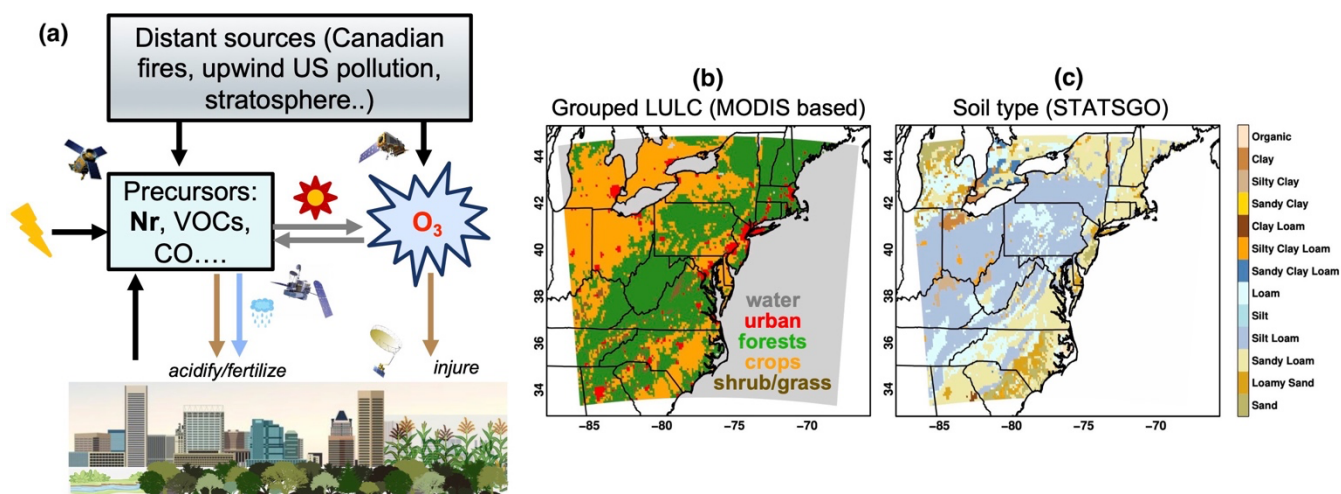
Figures

Figure 1: (a) A simplified schematic representation of Nr-O₃ relationships in the Earth systems; **(b)** model domain and the grid-
dominant land use/land cover (LULC) classifications, grouped from the original 20-category International Geosphere-Biosphere
1085 Programme-modified Moderate Resolution Imaging Spectroradiometer using the same criteria as in Huang et al. (2022); and **(c)**
the grid-dominant soil type based on the State Soil Geographic dataset. The grouped LULC is used for reporting potential O₃ and
Nr ecosystem impacts in Section 3.2, and approximately 32%, 24%, 1%, 3%, and 40% of model grids belong to the grouped
forests, crops, shrub/grass, urban, and water category, respectively.
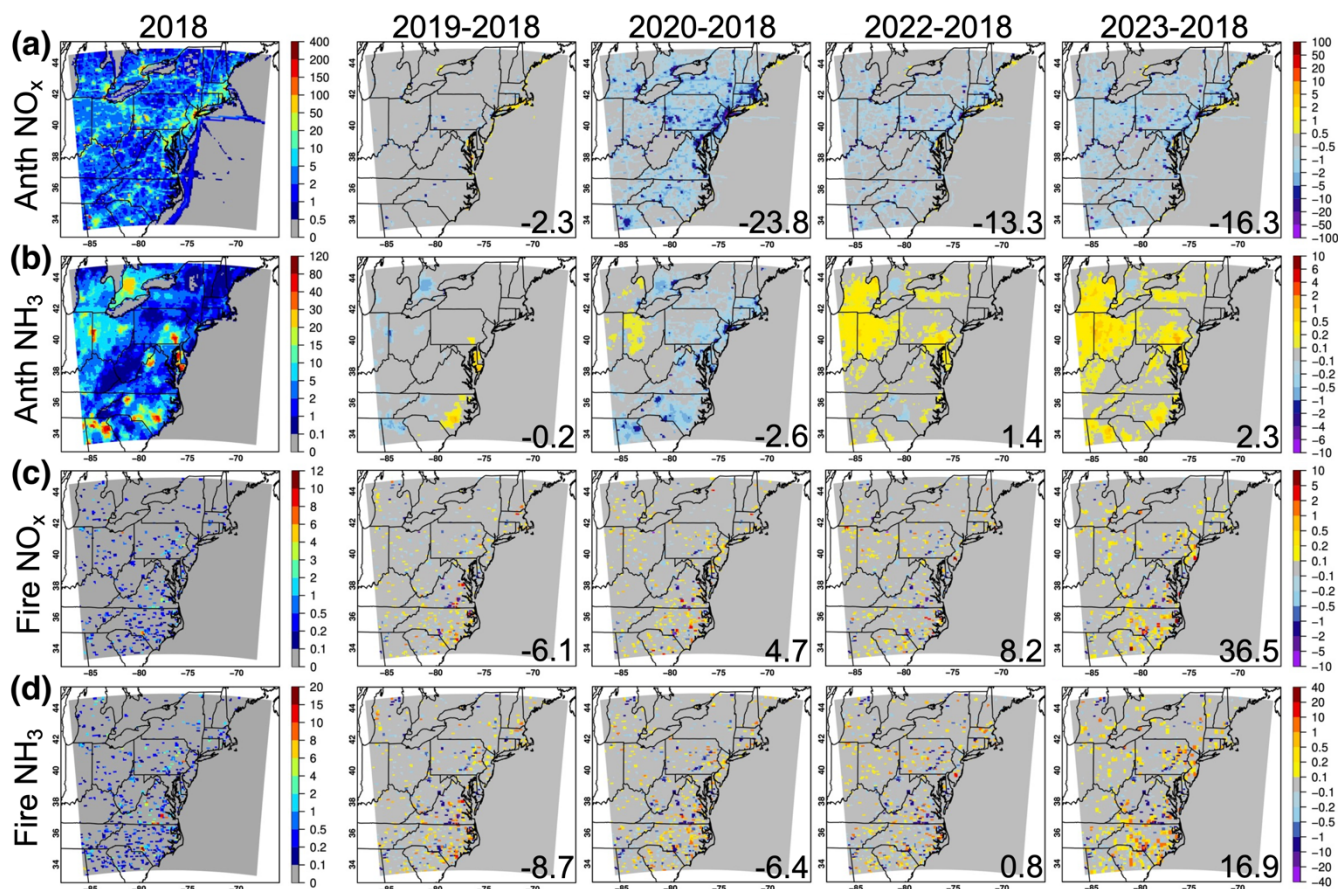
Figure 2: (a;b) Anthropogenic (Anth) and (c;d) biomass burning (fire) (a;c) NO$_x$ and (b;d) NH$_3$ emissions for MJJ 2018 and the differences between MJJ of each of the following years and 2018, in mol km^{-2} h^{-1}. Numbers at the corners of the difference plots indicate the % changes relative to MJJ 2018.
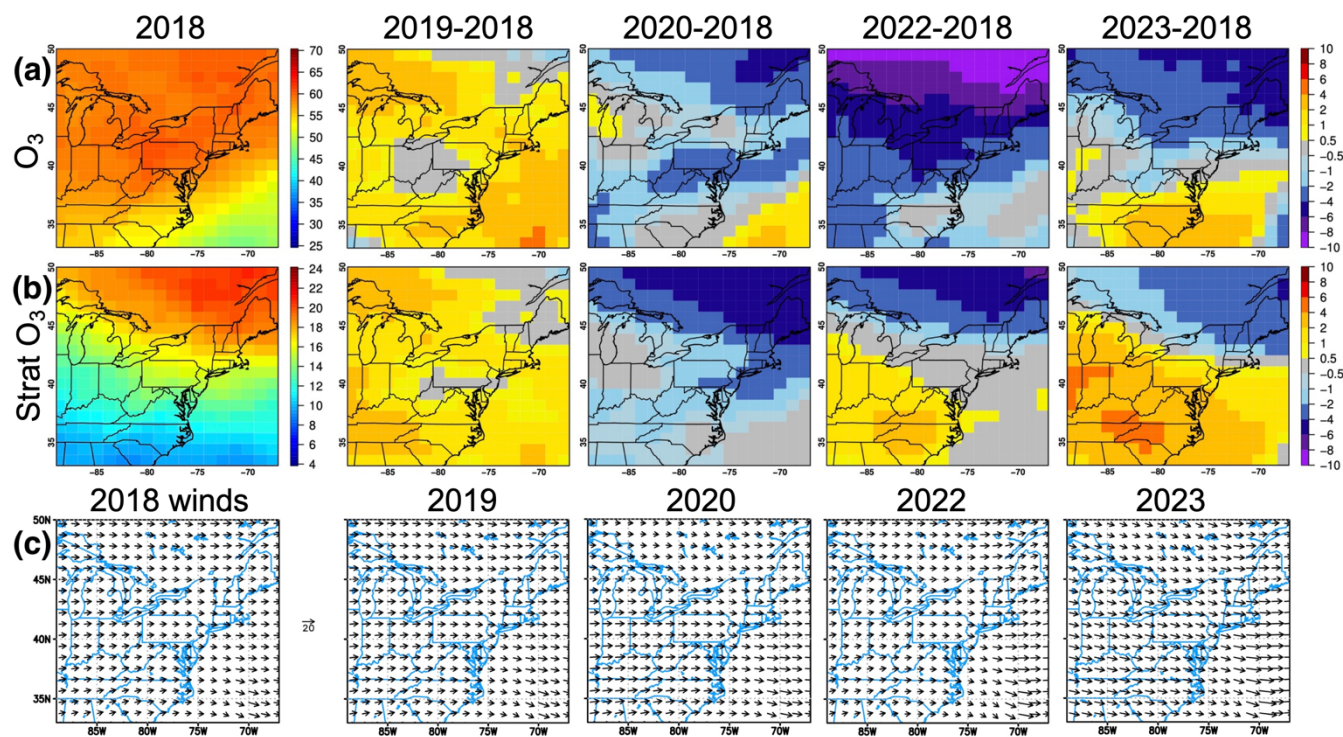
Figure 3: MJJ ~600–800 hPa (a) total and (b) stratospheric O₃ and their interannual differences in ppbv, and (c) wind fields for each year's MJJ, from WRF-Chem's chemical boundary condition models. Stratospheric O₃ impacts on the surface are indicated in Fig. S1.
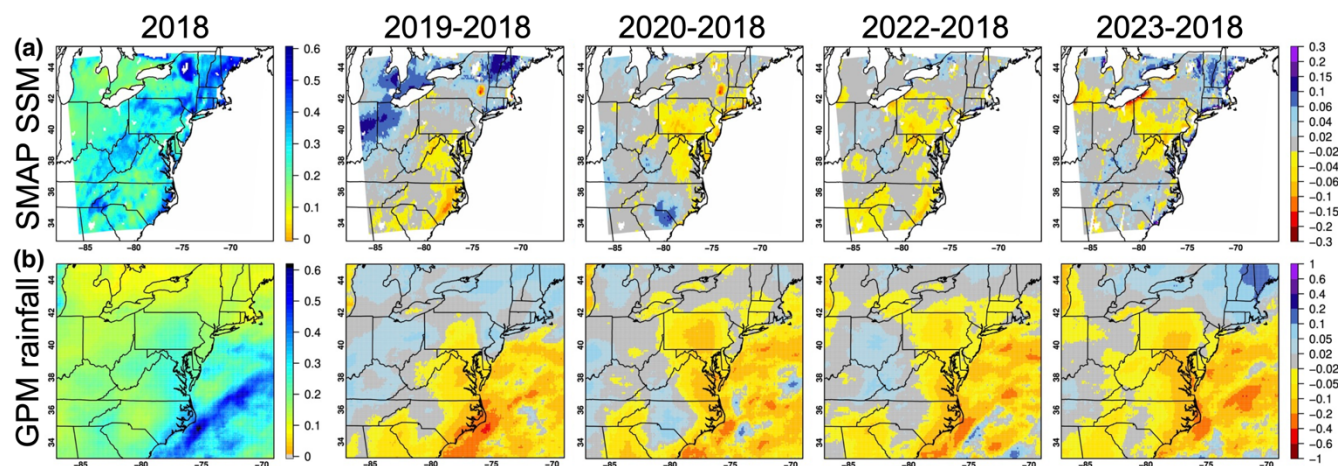
Figure 4: (a) SMAP morning-time SSM (m³ m⁻³) on WRF-Chem grids and (b) GPM/IMERG precipitation (mm h⁻¹) on its native grid for MJJ 2018 (left) and the differences between MJJ of each of the following years and 2018. SMAP measures the globe every 2–3 days and GPM daily global-coverage products are used for this work. SMAP data are not available during 20 June–22 July 2019 due to instrument outages; and the ESA CCI version 8.1 SM product indicates qualitatively similar MJJ 2019-2018 variability.
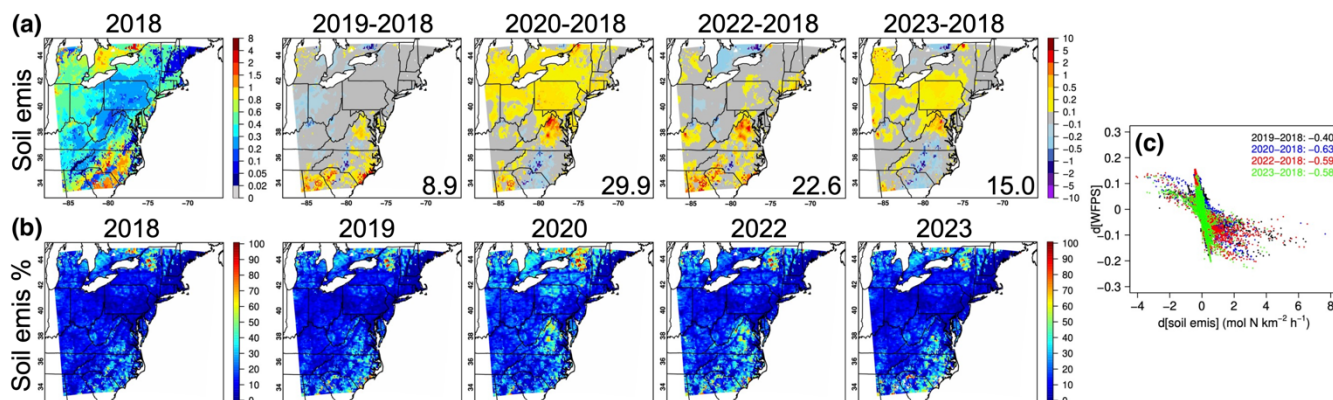
Figure 5: (a) Modeled soil NO and HONO emissions (mol N km^{-2} h^{-1}) and (b) soil NO and HONO emission % contributions to total anth+fire+soil NO$_y$ emissions. Model results are averaged for MJJ 2018, shown together with the differences between MJJ of each of the following years and 2018. Numbers at the corners of the soil emission difference plots in (a) indicate the % changes relative to MJJ 2018. The scatterplot in (c) indicates relationships between the interannual differences in water-filled pore space (WFPS, whose spatial patterns are shown in Fig. S3) and soil NO$_y$ emissions including their correlation coefficients in the upper-right legend (p<<0.01).
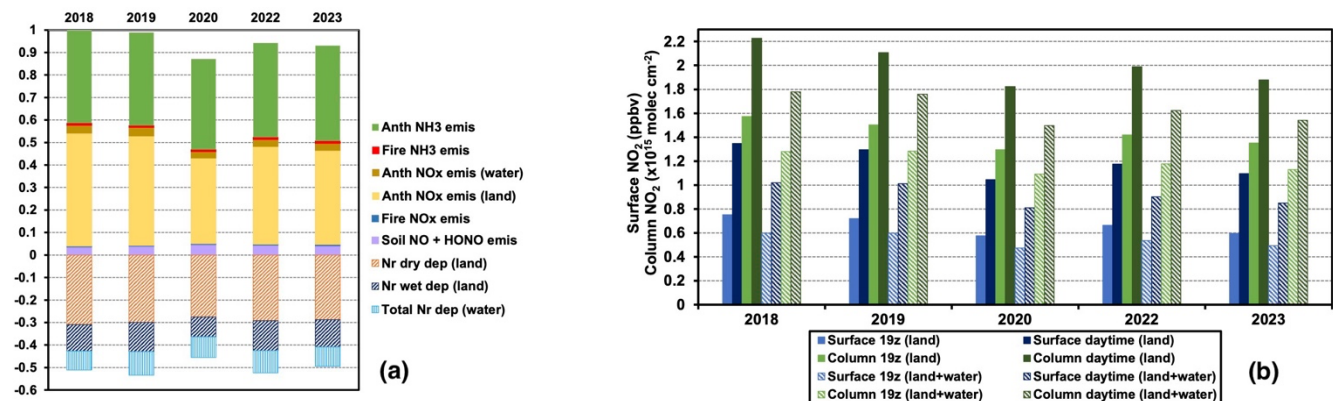
Figure 6: (a) Emission and deposition plots by year, scaled to MJJ 2018 total emissions; (b) Domain-wide MJJ-average surface and column NO$_2$, summarized for early-afternoon (19 UTC) and daytime, and for land and all model grids.
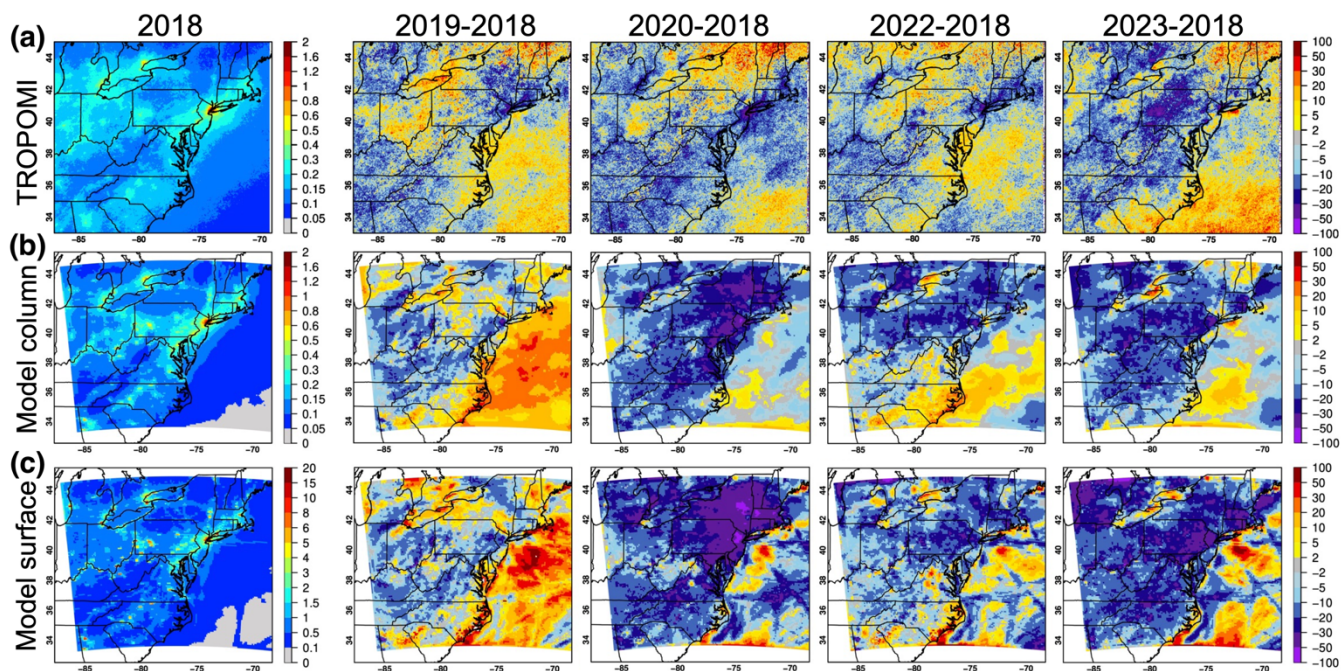
Figure 7: (a) TROPOMI and (b) WRF-Chem NO₂ columns; and (c) WRF-Chem surface NO₂. Results are averaged for MJJ 2018 (left, in ×10¹⁶ molec. cm⁻² for column NO₂ and ppbv for surface NO₂) and shown together with the % differences between MJJ of each of the following years and 2018.

1120
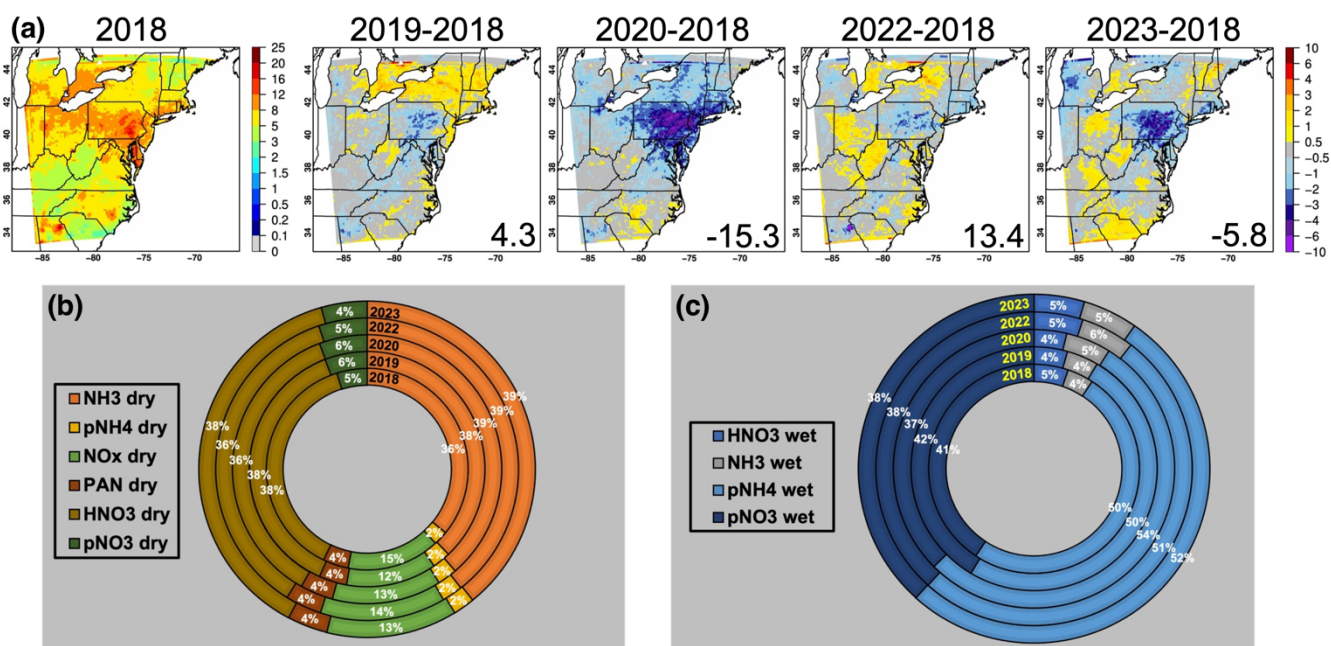
Figure 8: (a) Modeled MJJ 2018 total Nr deposition overland and differences between MJJ of each of the following years and 2018 in kgN ha⁻¹ a⁻¹; and speciation of modeled (b) dry and (c) wet deposition fluxes by year, where prefix "p" indicates particle.
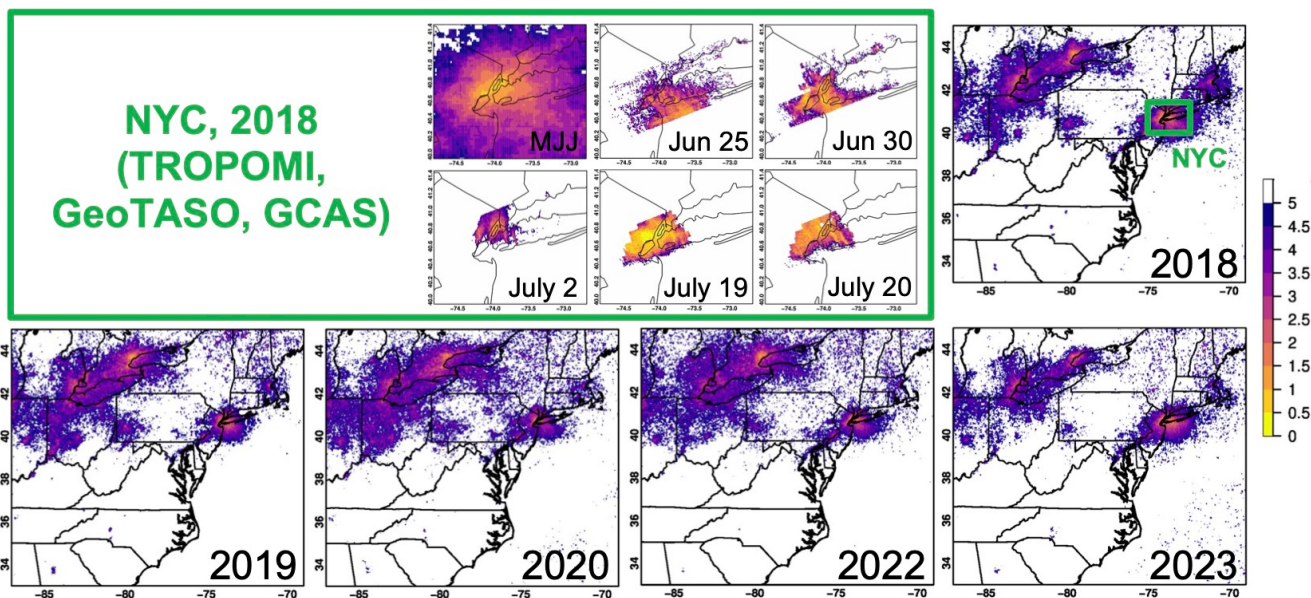
Figure 9: TROPOMI (MJJ 2018–2023), GeoTASO (25 and 30 June 2018) and GCAS (2, 19 and 20 July 2018) HCHO/NO₂ ratios. GeoTASO and GCAS both took measurements over the Greater New York City (NYC) several times during the sampling days which indicate subdaily variability in HCHO, NO₂ and their ratio. Their measurements closest to 19 UTC are used here.
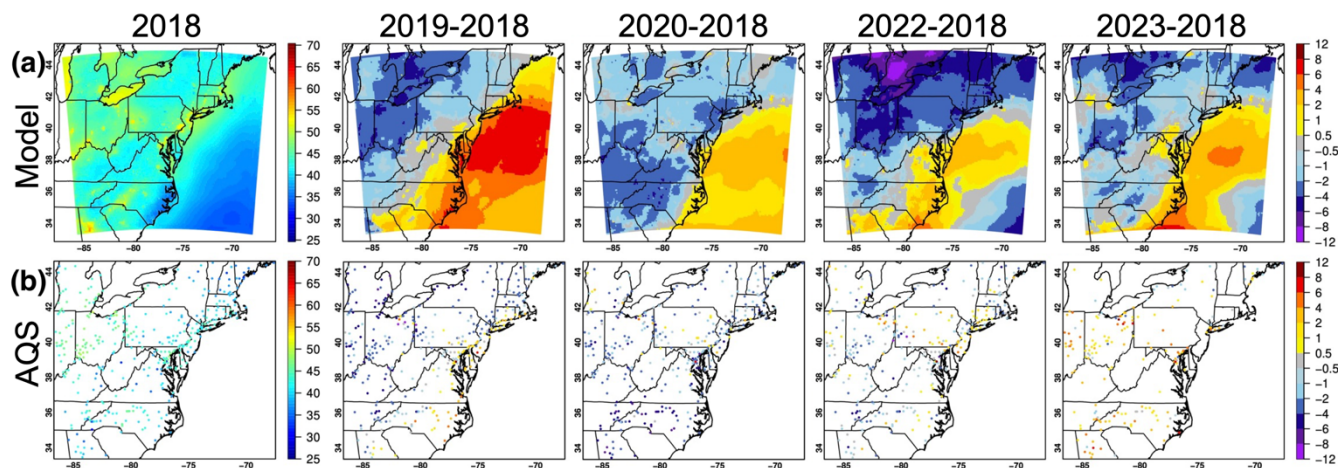
Figure 10: (a) WRF-Chem modeled and (b) AQS daytime surface O₃. Results are averaged for MJJ 2018, shown together with the differences between MJJ of each of the following years and 2018, all in ppbv. Observations from the AQS sites having <10% missing data for each year were used for evaluation. Model vs. AQS RMSEs (number of grids having collocated observations) for 2018, 2019, 2020, 2022, 2023 are 5.6 (375), 6.5 (377), 5.9 (373), 4.8 (370), 4.1 (201), respectively.
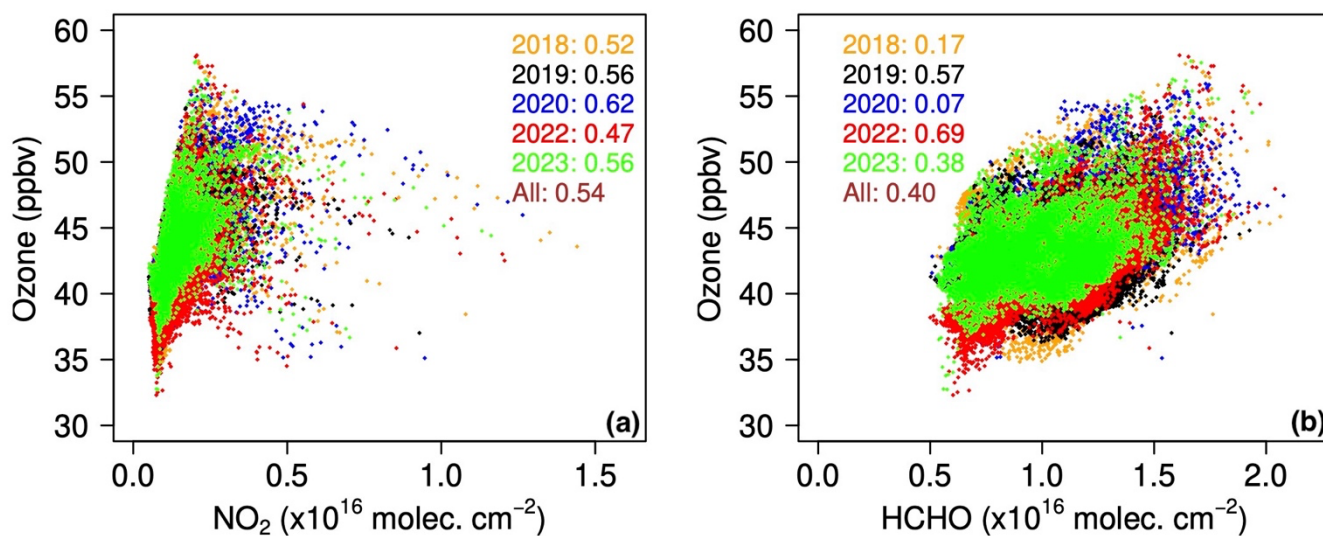
Figure 11: Scatterplots indicating WRF-Chem modeled (a) daytime-mean surface O₃ vs. 19 UTC NO₂ column and (b) daytime-mean surface O₃ vs. 19 UTC HCHO column relationships by year, for all terrestrial model grids. Their correlation coefficients (*p*<<0.01) are indicated in the corner legends.
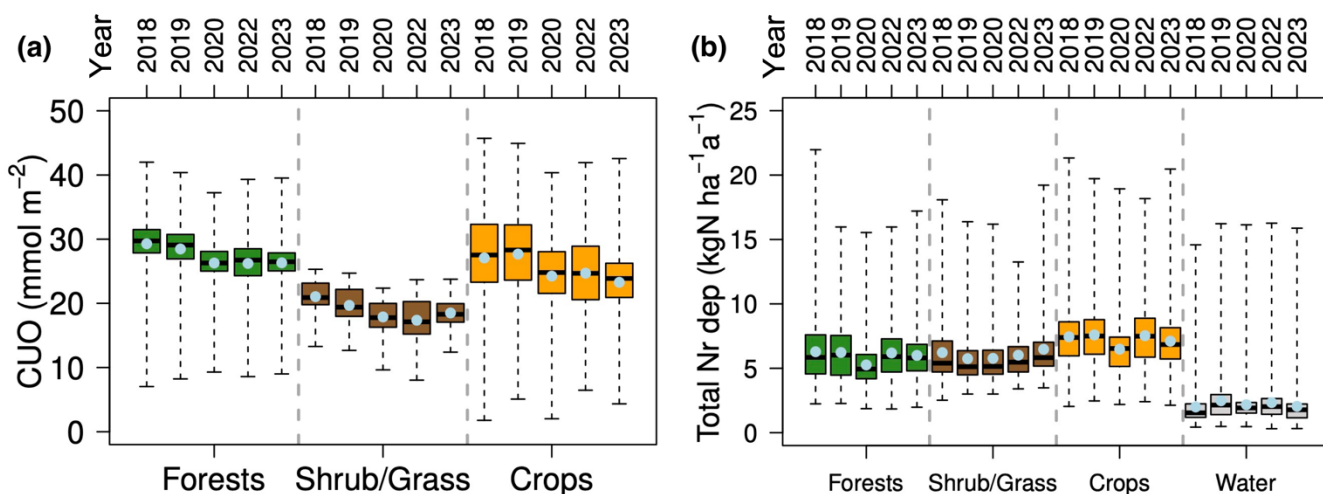
Figure 12: Box-and-Whisker plots of (a) CUO and (b) mean total Nr deposition fluxes for MJJ 2018–2023 by the grouped surface types defined in Fig. 1b.
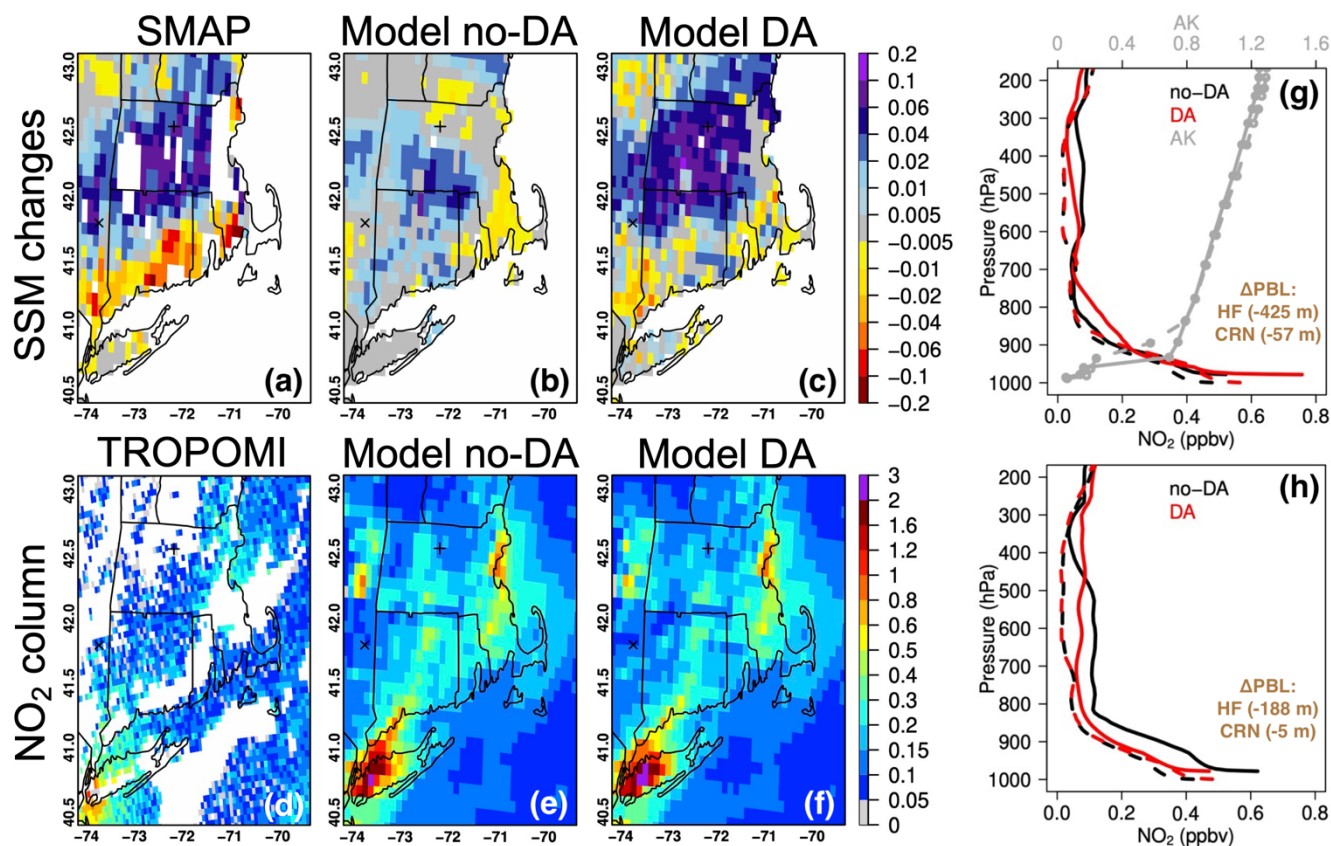
Figure 13: (a–c) 14 July-11 July SSM (m³ m⁻³) changes indicated by bias-corrected SMAP, free-running and SMAP-constrained Noah-MP results; (d–f) 14 July TROPOMI NO₂ columns (×10¹⁶ molec. cm⁻²) collected between 18–19 UTC, free-running and SMAP-constrained WRF-Chem results at 18 UTC; NO₂ vertical profiles from free-running and SMAP-constrained WRF-Chem at Harvard Forest (HF, solid line) and CRN-Millbrook (dash line) at (g) 18 UTC and (h) 19 UTC on 14 July, along with the impact of SMAP DA on modeled boundary layer height as well as TROPOMI averaging kernels (AK) on TROPOMI's *a priori* model grid. The + and × signs in (a–f) denote the locations of HF and CRN-Millbrook where in-situ precipitation and SSM data are also analyzed. Ground-based SSM measurements on 11 July and 14 July near SMAP overpasses are 0.170±0.059 and 0.245±0.080 m³ m⁻³ at HF, and 0.067 and 0.086 at CRN-Millbrook, respectively. Precipitation and ground-based O₃ observations on 11 and 14 July are shown in Fig. S10.
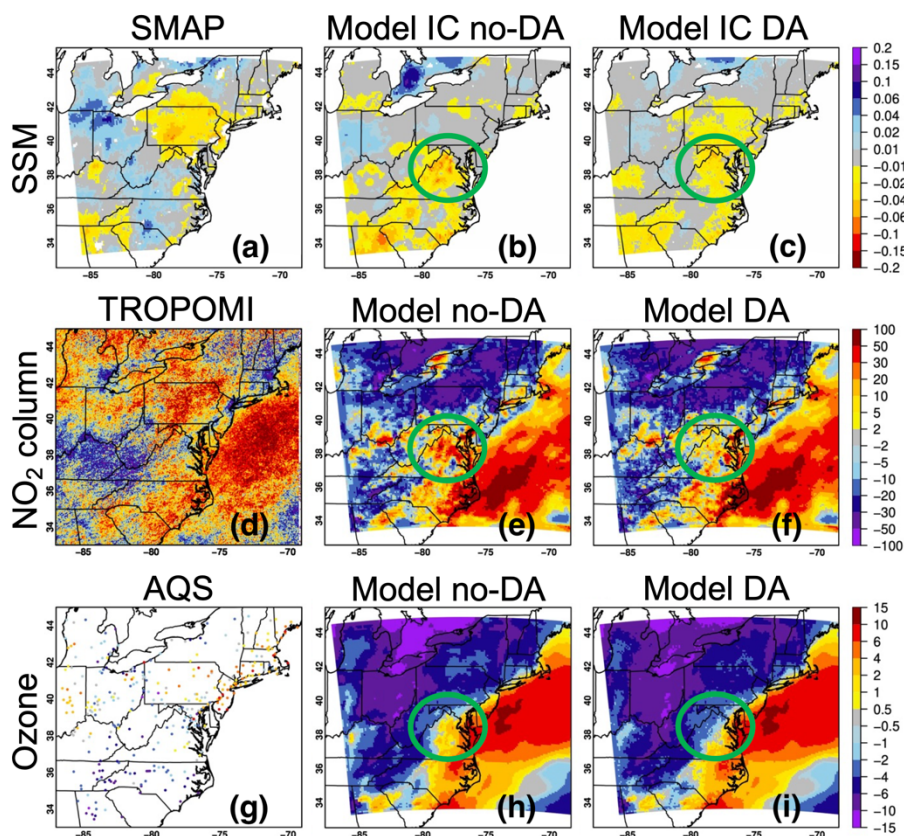
Figure 14: July 2022-July 2018 monthly differences in (a–c) SSM (m³ m⁻³) indicated by bias-corrected SMAP, free-running and SMAP-constrained WRF-Chem initial conditions (ICs); (d–f) early afternoon NO₂ columns (%) based on TROPOMI, free-running and SMAP-constrained WRF-Chem results; and (g–i) daytime surface O₃ concentrations (ppbv) based on AQS observations, free-running and SMAP-constrained WRF-Chem results. Green circles highlight areas in/around Virginia where improvements in WRF-Chem land ICs notably improved the NO₂ and O₃ fields.
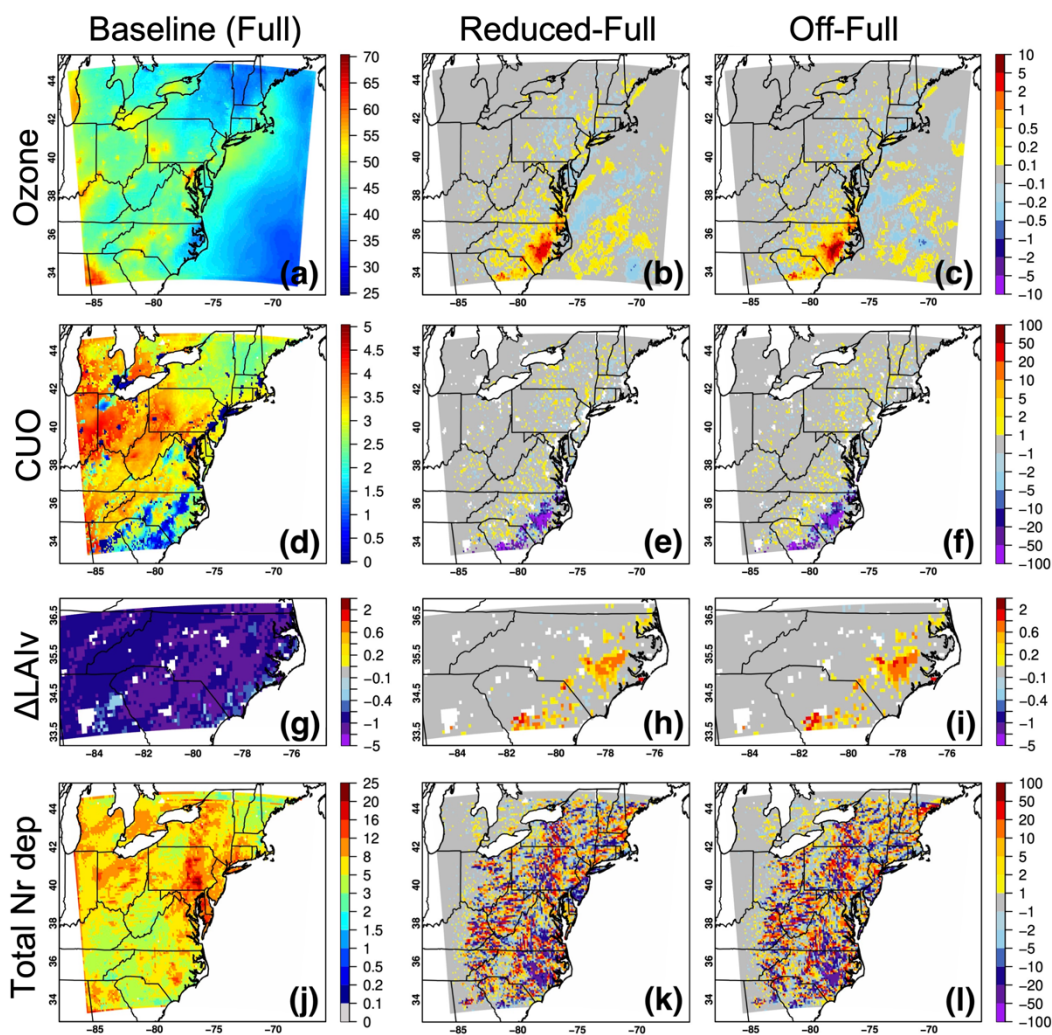
Figure 15: (a) Daytime surface O$_3$ concentration (ppbv, with the RMSE relative to AQS data of ~5.6 ppbv); (d) period-cumulated O$_3$ stomatal uptake (mmol m^{-2}); (g) O$_3$ impacts on leaf biomass (%) over irrigated areas in/around the Carolinas; and (h) total Nr deposition overland (kgN ha^{-1} a^{-1}) from the baseline simulation during 21–30 June 2022, and (b;c;e;f;h;i;k;l) their sensitivities to adjustments in irrigation schemes. Sensitivity results are in ppbv for surface O$_3$ concentration, and in % for all other plots.
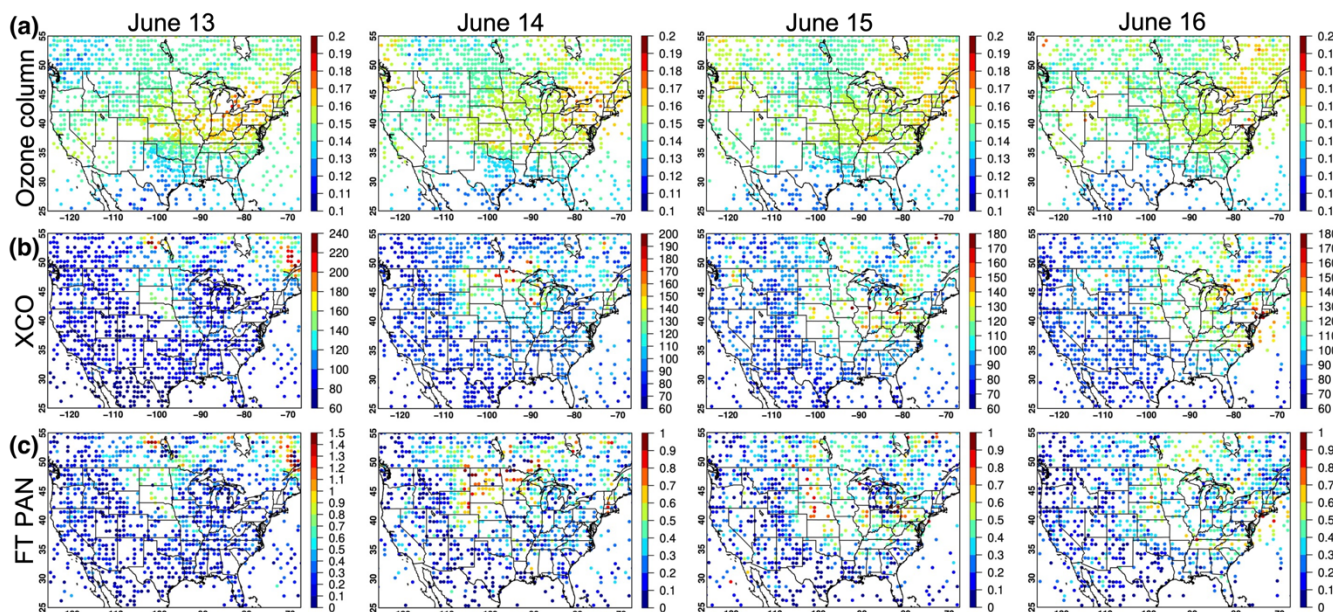
Figure 16: JPSS-1/CrIS observed (a) O₃ columns (mol m⁻²); (b) column-averaged CO mixing ratios (ppbv); and (c) column-averaged PAN mixing ratios (ppbv) for the free troposphere between 825 and 215 hPa, during 13–16 June 2023.
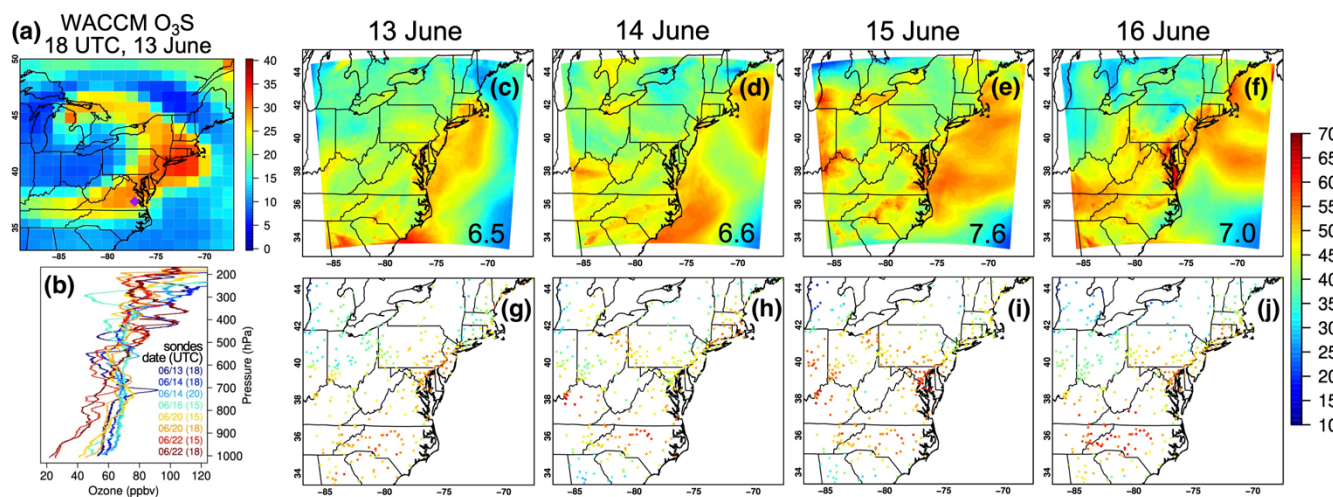
Figure 17: (a) WACCM model stratospheric O₃ tracer (ppbv) results at ~700h Pa at 18 UTC (local standard time + 5 or +6) of 13 June 2023, with location of the RRC site being indicated by the purple diamond; (b) Ozonesonde profiles launched from the RRC; and daytime surface O₃ concentrations (ppbv) on 13–16 June 2023 from (c–f) WRF-Chem and (g–j) AQS sites. WRF-Chem vs. AQS RMSEs (ppbv) are indicated in the lower-right corners of (c–f).
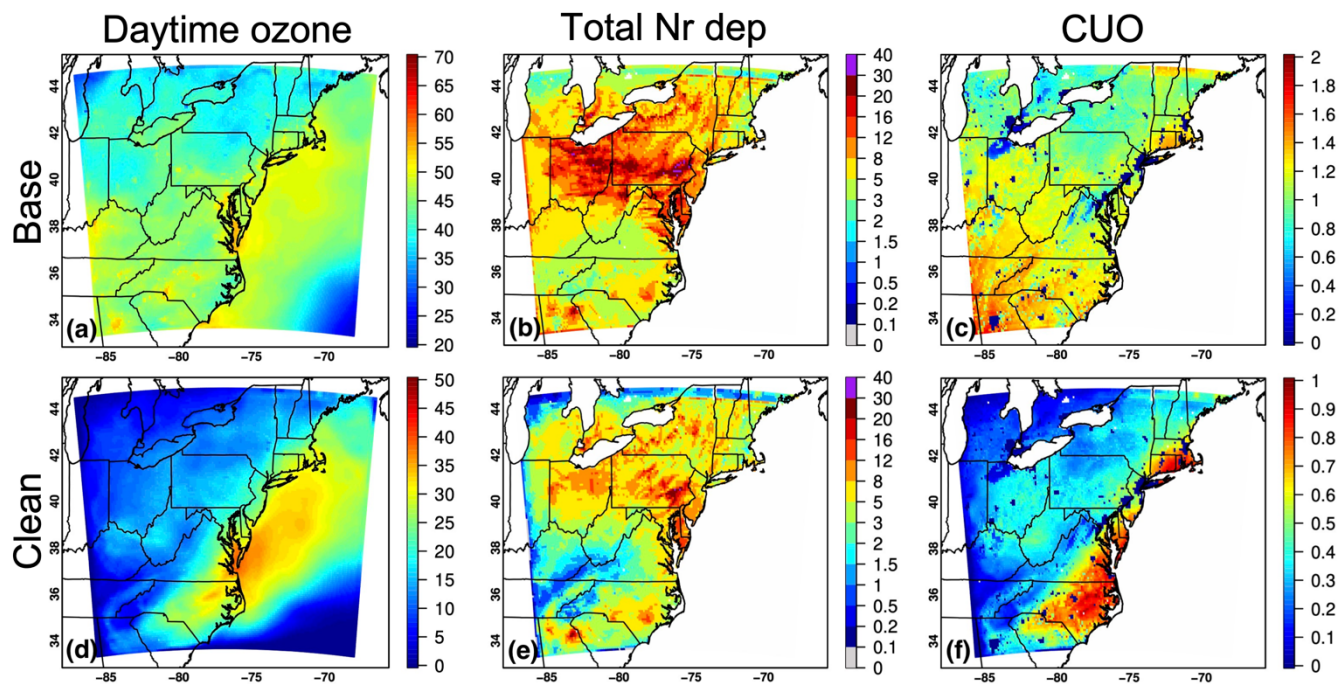
Figure 18: (a;d) Daytime surface O₃ concentrations (ppbv); (b;e) total Nr deposition overland (kgN ha⁻¹ a⁻¹); and (c;f) period-cumulated O₃ stomatal uptake (mmol m⁻²) during 13–16 June 2023 from the (a–c) baseline simulation and (d–f) sensitivity simulation with clean chemical BCs.